



The Global Structure of the Milky Way’s Stellar Halo Based on the Orbits of Local Metal-poor Stars

Genta Sato and Masashi Chiba

Astronomical Institute, Tohoku University, Aoba-ku, Sendai 980-8578, Japan; g.sato@astr.tohoku.ac.jp

Received 2021 August 24; revised 2022 January 2; accepted 2022 January 2; published 2022 March 10

Abstract

We analyze the global structure of the Milky Way (MW)’s stellar halo, including its dominant subcomponent, Gaia-Sausage-Enceladus (GSE). The method for reconstructing the global distribution of this old stellar component is to employ the superposition of the orbits covering the large MW’s space, where each of the orbit-weighting factors is assigned following the probability that the star is located at its currently observed position. The selected local, metal-poor sample with $[\text{Fe}/\text{H}] < -1$, using Gaia Early Data Release 3 and Sloan Digital Sky Survey Data Release 16, shows that the global shape of the halo is systematically rounder at all radii in more metal-poor ranges, such that an axial ratio, q , is nearly 1 for $[\text{Fe}/\text{H}] < -2.2$ and ~ 0.7 for $-1.4 < [\text{Fe}/\text{H}] < -1.0$. It is also found that a halo in the relatively metal-rich range of $[\text{Fe}/\text{H}] > -1.8$ actually shows a boxy/peanut-like shape, suggesting a major merger event. The distribution of azimuthal velocities shows a disk-like flattened structure at $-1.4 < [\text{Fe}/\text{H}] < -1.0$, which is thought to be the metal-weak thick disk. For the subsample of stars showing GSE-like kinematics, at $[\text{Fe}/\text{H}] > -1.8$, its global density distribution has an axis ratio of 0.9, which is more spherical than the general halo sample, and an outer ridge at $r \sim 20$ kpc. This spherical shape is consistent with the features of accreted halo components, and the ridge suggests that the orbit of GSE’s progenitor had an apocenter of ~ 20 kpc. Implications for the formation of the stellar halo are also presented.

Unified Astronomy Thesaurus concepts: Milky Way stellar halo (1060)

1. Introduction

It is generally thought that the stellar halo of the Milky Way (MW) contains the fossil record of the MW’s formation history imprinted in its kinematical and chemical properties. Since Eggen et al. (1962) showed a model of the MW’s formation process from the kinematic analysis of halo stars in the solar neighborhood, many studies of this Galactic fossil component have been carried out using a large number of newly available halo samples, with their assembly requiring considerable observational efforts over the past decades. These include, for example, the Hipparcos Catalog, obtained from the first astrometry satellite (Perryman et al. 1997), and spectroscopic catalogs such as RAVE (Steinmetz et al. 2006), SEGUE (Yanny et al. 2009), LAMOST (Cui et al. 2012; Zhao et al. 2012), GALAH (De Silva et al. 2015), APOGEE (Majewski et al. 2017), H3 (Conroy et al. 2019), and more. Perhaps the most significant impacts on this field of research have been brought about by the second astrometry satellite, Gaia. The Gaia catalog (Gaia Collaboration et al. 2016, 2018, 2021) provides trigonometric parallaxes and proper motions for billions of Galactic stars with unprecedented high accuracy. Based on the astrometry data of the stars in the Gaia catalog combined with that of the spectroscopic catalogs, the MW’s new dynamical maps have been drawn (e.g., Belokurov et al. 2018; Helmi et al. 2018; Myeong et al. 2018a, 2018b; Beane et al. 2019; Hagen et al. 2019; Iorio & Belokurov 2019; Anguiano et al. 2020; Cordoni et al. 2021; Koppelman et al. 2021), and new aspects of the MW’s formation and evolution history have been revealed (e.g., Antoja et al. 2018; Sestito

et al. 2019; Wyse 2019). In particular, the Gaia catalog has enabled the discovery of new substructures in the MW’s stellar halo (e.g., Koppelman et al. 2019; Myeong et al. 2019; Li et al. 2020) that are remnants of past merging/accretion events associated with the MW’s formation history (e.g., Fernández-Trincado et al. 2020; Naidu et al. 2020, 2021).

This observational information about the MW’s stellar halo has been investigated in comparison with various numerical simulations that produce a number of theoretically predicted halo structures in MW-sized galaxies, including their global density profiles and dynamical motions over a large halo space (e.g., Rodríguez-Gomez et al. 2016; Monachesi et al. 2019; Liang et al. 2021), as well as the merging/accretion history of satellite galaxies (e.g., Cooper et al. 2010; Mackereth et al. 2019; Kruijssen et al. 2020; Santistevan et al. 2020).

One of the most significant substructures in the MW’s stellar halo revealed by the Gaia catalog is Gaia-Sausage-Enceladus (GSE; Belokurov et al. 2018; Helmi et al. 2018). GSE shows an elongated distribution in a velocity space with azimuthal velocities of $v_\phi \sim 0$, and it is thought to be a tracer of a merger event with an SMC-class galaxy during the MW’s evolution about 10 Gyr ago (Helmi et al. 2018). Further details of GSE’s dynamical and chemical properties have been determined observationally (e.g., Feuillet et al. 2020; Monty et al. 2020), and several simulations have also been explored to constrain the properties of GSE’s progenitor (e.g., Bignone et al. 2019; Koppelman et al. 2020; Kim et al. 2021). Evans et al. (2020) showed that a merger event with a GSE-like progenitor is rare for MW-like galaxies. Thus, GSE is a unique feature of the MW’s stellar halo, thereby suggesting that the merger should be essential to the MW’s evolution history.

In previous observational studies, the stellar sample that is selected and used in the dynamical analysis is generally confined to the local volume of the Galactic space, so the

global structure of the stellar halo is hardly derived. For example, the region for which the Gaia catalog obtains accurate parallax data is limited to near the Sun, within heliocentric distances of ~ 4 kpc (see Section 2.1). To solve this issue and derive the spatial distributions of halo stars over a large Galactic space, we adopt the method based on stellar orbits (May & Binney 1986; Sommer-Larsen & Zhen 1990; Chiba & Beers 2000, 2001). Based on the superposition of stellar orbits, this method is designed to reconstruct the stellar distribution over a large region, up to the apocentric distances that stars can reach. Chiba & Beers (2000) used about 1200 metal-poor stars mostly selected from the Hipparcos catalog for this method. To go a step further in this work, we adopt Gaia Early Data Release 3 (EDR3; Gaia Collaboration et al. 2021) in combination with the spectroscopic information from Sloan Digital Sky Survey Data Release 16 (SDSS DR16) SEGUE, which allows us to have a much larger number of stars with better astrometric accuracy. Thus, it is expected that our reconstruction of the global halo distribution, over $r \sim 30$ kpc, will be more accurate and statistically more significant than previous studies.

Moreover, we also apply this method to the stars showing GSE-like kinematics, and derive GSE's global structure in the Galactic halo. In contrast to previous works (e.g., Feuillet et al. 2020; Monty et al. 2020), which investigated GSE's properties based on their local observational information, we adopt a strategy that uses the superposition of the orbits of GSE-like member stars to construct GSE's global distribution for the first time.

This paper is organized as follows. Section 2 explains the observational data with the selection conditions we adopt and the method for reconstructing the distribution of the MW's stellar halo as well as the GSE-like subsample. In Section 3, we show the structure of the reproduced global halo distribution and the results of the fitting to an ellipsoidal profile characterized by an index of the power-law radial profile, α , and an axial ratio, q . In Section 4, we discuss the implications from the derived distribution and structures of the stellar halo, and infer, based on the current results, the MW's formation and evolution history. Section 5 summarizes our work and conclusions.

2. Method

2.1. Data

We adopt the Gaia EDR3 Catalog (Gaia Collaboration et al. 2021) for astrometry data and the SDSS DR16 SEGUE catalog (Ivezić et al. 2008; Jurić et al. 2008; Bond et al. 2010) for spectroscopic data. We extract the common stellar data from these catalogs, which must satisfy the following five conditions to be adopted for our analysis.

The first condition is that the stellar metallicity $[\text{Fe}/\text{H}]$ is more metal-poor than -1 . This condition is to select stars belonging to the fiducial stellar halo, having low metals and possibly old ages.

The second and third conditions are that the effective temperature and the surface gravity of a star are within the range $4500 < T_{\text{eff}} < 7000$ K and $3.0 < \log g < 5.2$, respectively. These constraints are to extract the main-sequence stars, following the work of Ivezić et al. (2008), which also derived the range of the observational quantities that fulfill main-sequence stars.

The fourth and fifth conditions are for ensuring the accuracy of the data, i.e., to avoid stars having large uncertainties in parallaxes and metallicities, respectively. We select the stars for which the relative uncertainty of the parallax σ_{ϖ}/ϖ is smaller than 0.2 and the uncertainty of $[\text{Fe}/\text{H}]$ is smaller than 0.1 dex.

Next, we carry out crossmatching between these two catalogs using the CDS Xmatch Service,¹ where the cross-matching condition for the stellar position is given as being smaller than $1''$. Setting only this positional condition, however, leaves some cases where a few SDSS stars match with a single Gaia star. In such cases, we impose an additional condition for the photometry of stars, following the relation between the G band used in Gaia and the (g, i) bands in SDSS (Busso et al. 2021):

$$G - g = -0.1064 - 0.4964(g - i) - 0.09339(g - i)^2 + 0.004444(g - i)^3. \quad (1)$$

We adopt the star with the smallest magnitude difference among the position-matched candidate stars between the two catalogs.

The spectroscopic catalog (SDSS SEGUE) is used to extract the line-of-sight velocities and spectroscopic metallicities of the sample stars. The stars that have this spectroscopic information with good accuracy are limited to only bright ones, so the range of the G -band absolute magnitude of our sample is $M_G \lesssim 8$ mag.

We have extracted 25,093 stars as the fiducial members of the stellar halo.² The distributions of these stars are shown in Figure 1. In the following, we divide the sample stars into four main subsamples, based on their metallicities: $-1.4 < [\text{Fe}/\text{H}] < -1.0$; $-1.8 < [\text{Fe}/\text{H}] < -1.4$; $-2.2 < [\text{Fe}/\text{H}] < -1.8$; and $[\text{Fe}/\text{H}] < -2.2$ (shown with different colors in Figure 1 and the following figures). The number of stars in each subsample is 10,214, 8484, 4518, and 1877, respectively.

Additionally, we also consider the likely member stars belonging to GSE. The GSE stars are distributed around the azimuthal velocities, v_ϕ , near 0 (Myeong et al. 2018a; Belokurov et al. 2018), which corresponds to the vertical angular momentum L_z as small as 0. We note that strongly bound stars, namely stars with low orbital energy, are dominated by the so-called in situ halo component (e.g., Naidu et al. 2020), and such stars are not GSE members. Thus, we extract the GSE-like stars that fulfill the conditions regarding the binding energy E and the vertical angular momentum L_z : $E > -150,000 \text{ km}^2 \text{ s}^{-2}$ and $-500 < L_z < 500 \text{ kpc km s}^{-1}$ (see Section 2.2.1 for the definitions of E and L_z). The number of extracted stars is 9402.

These stars belonging to the GSE-like members are also divided into four subsamples, depending on their metallicity ranges, of $-1.4 < [\text{Fe}/\text{H}] < -1.0$, $-1.8 < [\text{Fe}/\text{H}] < -1.4$, $-2.2 < [\text{Fe}/\text{H}] < -1.8$, and $[\text{Fe}/\text{H}] < -2.2$, where the numbers of stars are 3269, 3607, 1827, and 699, respectively. Although the real GSE may dominate in the intermediate metallicity range, e.g., $-1.66 < [\text{Fe}/\text{H}] < -1.33$ (Belokurov et al. 2018), covering our subsample of $-1.8 < [\text{Fe}/\text{H}] < -1.4$, we also consider other metallicity ranges to analyze the metallicity dependence of the GSE-like structure and to compare them with the general distribution of the stellar halo.

¹ <http://cdsxmatch.u-strasbg.fr>

² In comparison, Kim & Lépine (2022) recently adopted $\sim 500,000$ thick-disk and halo-like stars with $M_G < 13$ mag to analyze their reduced proper motions without the limitations of the availability of the spectroscopic data.

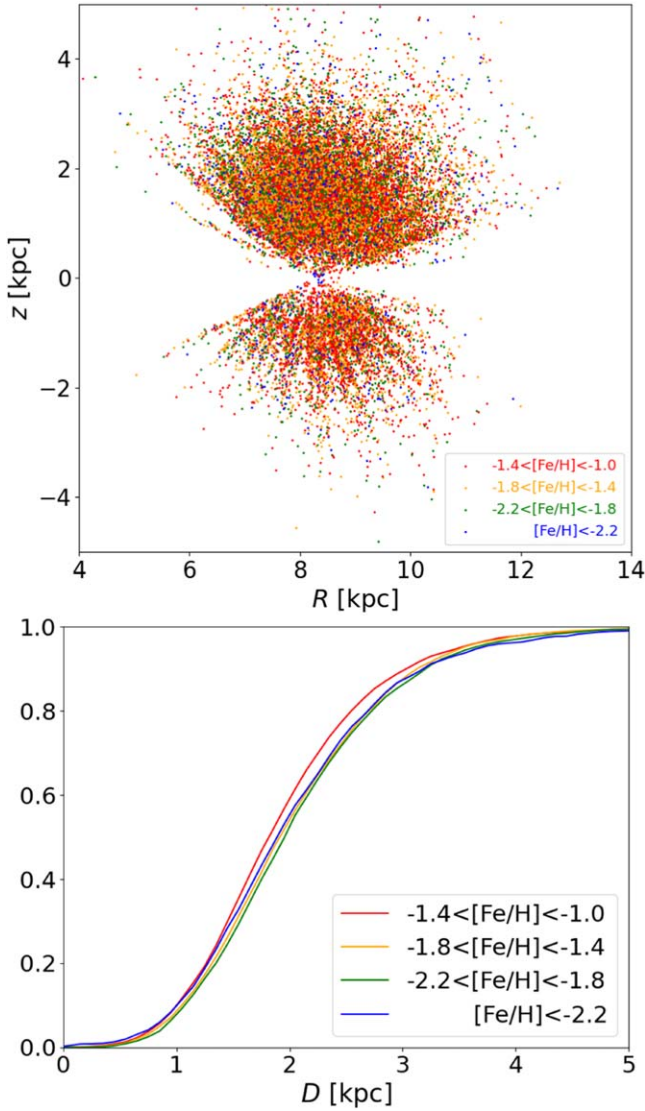


Figure 1. Upper panel: the meridian distribution of the fiducial metal-poor halo stars adopted in this work selected from the crossmatching of the Gaia EDR3 and SDSS DR16 SEGUE catalogs. The different colors correspond to the different ranges of stellar metallicities: red for $-1.4 < [\text{Fe}/\text{H}] < -1.0$; orange for $-1.8 < [\text{Fe}/\text{H}] < -1.4$; green for $-2.2 < [\text{Fe}/\text{H}] < -1.8$; and blue for $[\text{Fe}/\text{H}] < -2.2$. This correspondence is applied in the following figures. Bottom panel: the cumulative number distribution of the heliocentric distance, D , for the adopted stellar sample divided by the metallicity ranges. The histograms are normalized so that the total number is 1 for each range.

2.2. Dynamical Model

We adopt the method based on the superposition of the discrete stellar orbits to reproduce and analyze the global distribution of the MW’s stellar halo, following the seminal works by May & Binney (1986) and Sommer-Larsen & Zhen (1990). Although the Gaia catalog provides billions of astrometric data, stars with accurate parallaxes of $\sigma_{\varpi}/\varpi < 0.2$ are only available in the local volume near the Sun, which is small compared with the entire MW’s halo space (Figure 1). By calculating the stellar orbits and their superposition with appropriate weighting, we can construct the MW’s halo distribution beyond the region where we can observe stars locally and individually. This subsection presents the adopted gravitational potential, the properties of the stellar orbits in it, and then the method for constructing the global distribution of the stellar halo from the orbits.

2.2.1. Gravitational Potential

In this work, for the purpose of calculating each orbital density analytically, as described below, we adopt the Stäckel form for the MW’s gravitational potential. The Stäckel potential, ψ , is generally expressed as

$$\psi(\lambda, \nu) = -\frac{(\lambda + \gamma)G(\lambda) - (\nu + \gamma)G(\nu)}{\lambda - \nu}, \quad (2)$$

where $G(\tau)$ is an arbitrary function (de Zeeuw 1985; Dejonghe & de Zeeuw 1988). λ and ν are the spheroidal coordinate system (λ, ν) , defined as the solution to the following equation for τ ,

$$\frac{R^2}{\tau + \alpha} + \frac{z^2}{\tau + \gamma} = 1, \quad (3)$$

where α and γ are constants and (R, z) are the Galactocentric cylindrical coordinates, assuming that the position of the Sun is $(R_{\odot}, z_{\odot}) \equiv (8.3 \text{ kpc}, 0)$ (Gillessen et al. 2009). The contours of $\lambda, \nu = \text{constant}$ describe ellipses and hyperbolas, respectively.

For the arbitrary function $G(\tau)$ in Equation (2), we consider the contribution of gravitational force from the stellar disk and dark halo components. Here we adopt a Kuzmin–Kutuzov potential (Dejonghe & de Zeeuw 1988; Batsleer & Dejonghe 1994; Chiba & Beers 2001) for both components given in the first and second terms below, respectively,

$$G(\tau) = \frac{G_{\text{grav}}kM}{\sqrt{\tau} + \sqrt{-\gamma}} + \frac{G_{\text{grav}}(1-k)M}{\sqrt{\tau+b} + \sqrt{-\gamma+b}}, \quad (4)$$

where G_{grav} is the gravitational constant, M is the total mass of the MW, k is the ratio of the disk mass to the total mass, and b is the parameter for making this two-component model in the Stäckel form.

In this work, we adopt $M = 10^{12}M_{\odot}$, which is nearly in agreement with several recent measurements, e.g., $0.7 \times 10^{12}M_{\odot}$ (Eadie & Jurić 2019), $1.3 \times 10^{12}M_{\odot}$ (Grand et al. 2019; Posti & Helmi 2019), $1.0 \times 10^{12}M_{\odot}$ (Deason et al. 2019), and $1.2 \times 10^{12}M_{\odot}$ (Deason et al. 2021). For the other parameters, k, α, γ , and b , we take the same values as those in Chiba & Beers (2001) so as to make the current model resemble the real galaxy: the circular velocity at $R > 4 \text{ kpc}$ is constant and $\simeq 220 \text{ km s}^{-1}$, the local mass density at $R = R_{\odot}$ is $0.1 \simeq 0.2 M_{\odot} \text{ pc}^{-3}$, and the surface mass density at $R = R_{\odot}$ is $70 M_{\odot} \text{ pc}^{-2}$ within $z \lesssim 1.1 \text{ kpc}$. We adopt $k = 0.09$ for the disk fraction, and α and γ are associated with the disk’s scalelength in R , a_D , and scaleheight in z , c_D , respectively, as $\alpha = -a_D^2$ and $\gamma = -c_D^2$. The corresponding scales for the dark halo, a_H and c_H , are set as $a_H^2 = a_D^2 + b$ and $c_H^2 = c_D^2 + b$, respectively. These values of scales are given as $c_D = 0.052 \text{ kpc}$, $c_H = 17.5 \text{ kpc}$, $c_D/a_D = 0.02$, and $c_H/a_H = 0.99$.

The rotation curve of this gravitational potential is shown in Figure 2. It captures the features that the rotational speed near the Sun, $R \sim 8 \text{ kpc}$, is about 220 km s^{-1} , and the curve farther than 8 kpc is almost flat. They are consistent with the observational properties (e.g., Mróz et al. 2019; Sofue 2020), so we believe this model is appropriate for the following analysis. It is true that the current Stäckel potential does not perfectly represent the actual Galactic potential, especially near the disk plane, in contrast to other models, such as MWPotential2014 (Bovy 2015). However, since we focus on the distribution of the stellar halo, which is mostly spread out

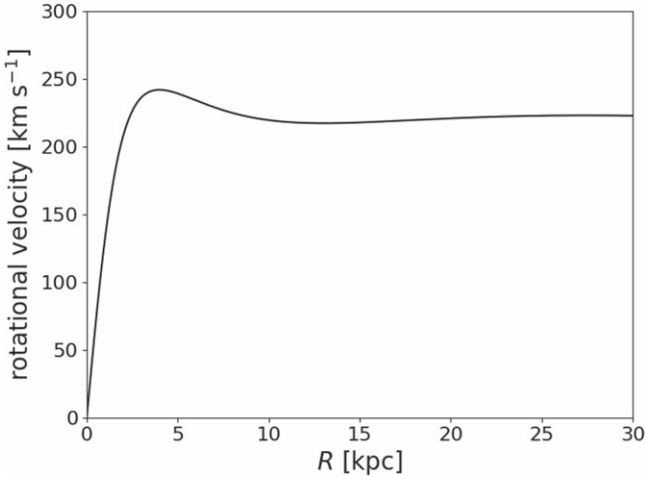


Figure 2. The rotation curve of the mass model adopted in this work, which is basically in agreement with the observed one in the MW.

widely in the high- z region, we consider that the difference of the potentials near the disk does not affect the result critically.

In this work, we define the heliocentric distance as the inverse of parallax. Bailer-Jones et al. (2021) showed a more accurate distance, considering the effects of extinction, magnitude, and color. We find that the difference between ϖ^{-1} and the distance of Bailer-Jones et al. (2021) lies within 1σ for 75% of our sample and within 2σ for 90%, under the condition of $\sigma_{\varpi}/\varpi < 0.2$. Thus, we regard the inverse of parallax as the distance in this work.

2.2.2. Stellar Orbits

The Stäckel potential has a unique feature that all three integrals of motion can be written analytically (de Zeeuw & Lynden-Bell 1985). This axisymmetric system allows three integrals of motion, (E , I_2 , I_3). E and I_2 are defined as

$$E = \frac{1}{2}|\mathbf{v}|^2 + \psi(\mathbf{x}) \quad (5)$$

$$I_2 = \frac{1}{2}L_z^2 \text{ with } L_z = Rv_\phi, \quad (6)$$

where v_ϕ is the azimuthal component of the velocity vector. The remaining third integral cannot generally be described analytically in any axisymmetric system, except for the case of a Stäckel potential. In the case of a Stäckel model, the third integral I_3 is expressed as

$$I_3 = \frac{1}{2}(L_x^2 + L_y^2) + (\gamma - \alpha) \left[\frac{1}{2}v_z^2 - z^2 \frac{G(\lambda) - G(\nu)}{\lambda - \nu} \right], \quad (7)$$

where (x, y, z) are the Cartesian coordinates with $x = R \cos \phi$ and $y = R \sin \phi$.

The distribution of our stellar data in phase space (E , I_2 , I_3) is shown in Figures 3 and 4. The rectangle in Figure 3 means that the stars inside it belong to the GSE-like subsample.

The physical meaning of I_3 is the generalized horizontal angular momentum L_{\parallel} : in a spherically symmetric case, two constants α and γ are equal, so $I_3 = (1/2)(L_x^2 + L_y^2) = (1/2)L_{\parallel}^2 = (1/2)(L^2 - L_z^2)$. The total angular momentum L is an integral of

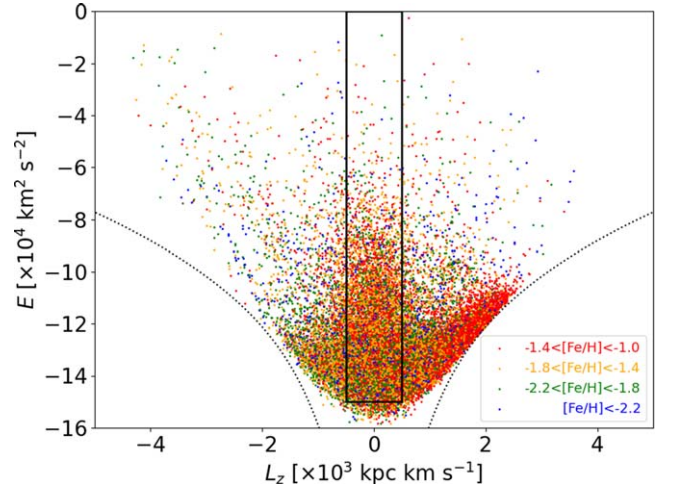


Figure 3. The phase-space (E , L_z) distribution of the fiducial halo stars adopted in this work. The black dotted line corresponds to a circular orbit, i.e., the lowest orbital energy, E , for a given vertical component of angular momentum, L_z . The rectangle indicates the selection region of the stars we have adopted as the GSE-like subsample.

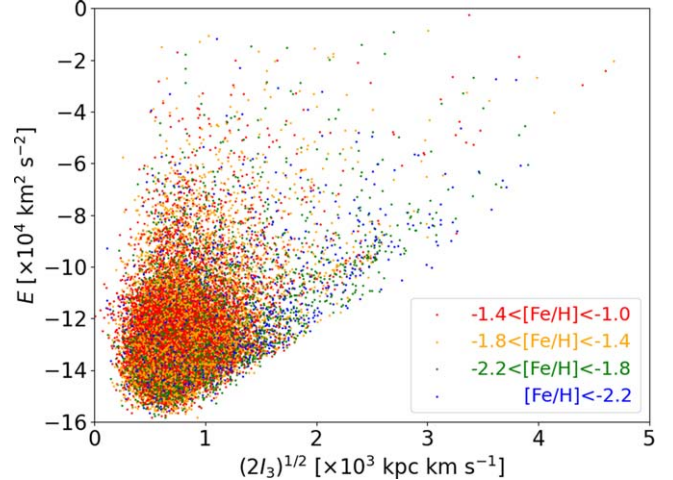


Figure 4. The distribution of the fiducial halo stars in the phase space ($\sqrt{2I_3}$, E). We note that $\sqrt{2I_3}$ has the dimension of angular momentum, and becomes $\sqrt{L_x^2 + L_y^2}$ in the case of a spherically symmetric gravitational potential.

motion in a spherical model, so L_{\parallel} is also an integral of motion. Therefore, $\sqrt{2I_3}$ can be regarded as the generality of L_{\parallel} (this is why the horizontal axis in Figure 4 describes $\sqrt{2I_3}$, not simply I_3).

It is known that I_3 has a correlation with the maximum inclination angle, θ_{\max} , of an orbit, where θ_{\max} is defined as the angle from the Galactic plane. Our θ_{\max} versus I_3 diagram is shown in Figure 5. We find that the correlation appears clearly. Additionally, Figure 6 shows the number distribution of θ_{\max} for the current sample stars. It suggests that the distribution is peaked at $\theta_{\max} \sim 15^\circ$ and smoothly declines at larger θ_{\max} .

Since the integrals of motion contain complete information about the orbit of a star, the fact that all integrals of motion are described analytically means that we can reproduce the stellar orbit accurately and completely. Under the Stäckel potential, the orbital density of the i -th star at position \mathbf{x} is expressed as (de Zeeuw 1985; Dejonghe & de Zeeuw 1988; Sommer-Larsen & Zhen 1990; Chiba & Beers 2001)

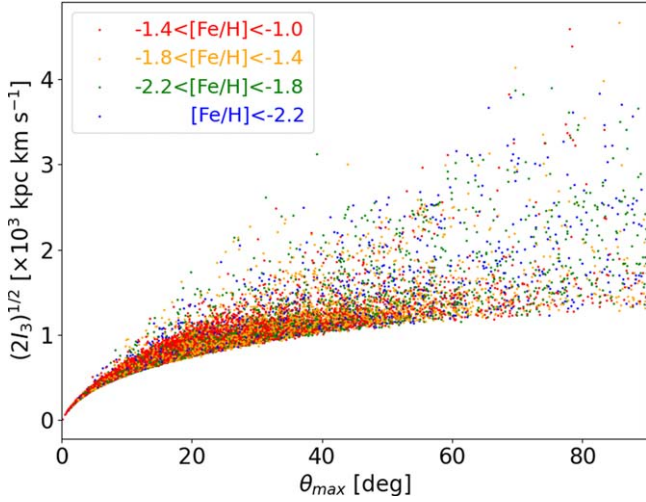


Figure 5. The correlation between the orbital angles measured from the Galactic plane, θ_{\max} , and $\sqrt{I_3}$ in the fiducial halo stars.

$$\rho_{\text{orb},i}(\mathbf{x}) = \frac{2\sqrt{2}}{R} \frac{1}{\sqrt{N_i(\lambda)(\lambda + \gamma)} \sqrt{N_i(\nu)(\nu + \gamma)} \sqrt{I_{2,i}}} \quad (8)$$

$$\text{where } N_i(\tau) = G(\tau) - \frac{I_{2,i}}{\tau + \alpha} - \frac{I_{3,i}}{\tau + \gamma} + E_i. \quad (9)$$

We reconstruct the density distribution of the sample halo stars, $\rho(\mathbf{x})$, by overlaying the orbital densities with proper weights, c_i .

$$\rho(\mathbf{x}) = \sum_{i=1}^N c_i \rho_{\text{orb},i}(\mathbf{x}). \quad (10)$$

Here, the orbit-weighting factors c_i are determined by a maximum likelihood method, as follows. When the i -th star has integrals of motion (E_i , $I_{2,i}$, $I_{3,i}$), the probability P_{ij} that the star is observed at the position \mathbf{x}_j is expressed as

$$P_{ij} = \frac{c_i \rho_{\text{orb},i}(\mathbf{x}_j)}{\sum_{k=1}^N c_k \rho_{\text{orb},k}(\mathbf{x}_j)}. \quad (11)$$

The i -th integrals of motion are calculated from the i -th observed star, so the case of $i=j$ realizes for any i . Therefore, the probability P_{ij} should be maximized at $i=j$ for arbitrary j . We define the weights c_i so that $\prod_{i=1}^N P_{ij}$ is maximized (Sommer-Larsen & Zhen 1990; Chiba & Beers 2000, 2001).

The orbit-weighting factors c_i are designed to be proportional to the inverse of the time that the i -th star spends at the currently observed position, or the inverse of the i -th orbital density at the position where the i -th star is observed, $\rho_{\text{orb},i}(\mathbf{x}_i)$.

$$c_i \propto \frac{1}{\rho_{\text{orb},i}(\mathbf{x}_i)} \quad (12)$$

This procedure means that a higher weight is given to a star located at the position of lower $\rho_{\text{orb},i}(\mathbf{x}_i)$ in the course of its orbital motion: since the probability of finding such a star at its current position is low, the fact that it is actually observed there leads to the assignment of a higher orbit-weighting factor c_i . Conversely, a lower c_i is assigned to a star currently located at higher $\rho_{\text{orb},i}(\mathbf{x}_i)$, e.g., near the edge of its orbit, where a star stays for a longer time.

In addition to the global density structure of metal-poor halo stars, we also construct their global rotational velocity

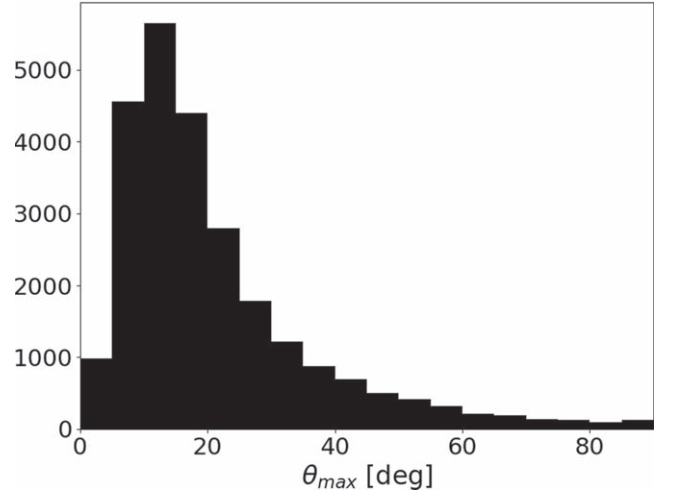


Figure 6. The distribution of the orbital angle, θ_{\max} . While the number of stars with $\theta_{\max} > 15^\circ$ shows a monotonous decrease with increasing θ_{\max} , the stars with $\theta_{\max} < 15^\circ$ are deficient from the extrapolation from this distribution.

distribution. We calculate the values of mean rotational velocity $\langle v_\phi \rangle$ as follows:

$$\langle v_\phi(\mathbf{x}) \rangle = \frac{1}{\rho(\mathbf{x})} \sum_i c_i \rho_{\text{orb},i}(\mathbf{x}) v_{\phi,i}(\mathbf{x}) \quad (13)$$

$$\text{where } v_{\phi,i}(\mathbf{x}) = \pm \sqrt{\frac{2I_{2,i}}{R^2}}. \quad (14)$$

The sign in Equation (14) is determined to match the rotational direction of the observational i -th star.

3. Results

In what follows, we show our results on the meridian plane using the coordinates (r, θ) and also the cylindrical coordinates (R, z) . The relation between these coordinates is $R = r \cos \theta$, $z = r \sin \theta$, so (r, θ) correspond to the two-dimensional polar coordinates where θ is measured from the Galactic plane.

3.1. The Entire Halo Sample

3.1.1. Density Distribution

The reproduced global density distribution of the halo sample expressed by Equation (10) is shown in Figure 7, where the total amplitude of the density is normalized by the value at $(R, z) = (10 \text{ kpc}, 0)$. The density contours hold nearly ellipsoidal shapes in all metallicity ranges, although the detailed contour pattern looks like a somewhat boxy or peanut-like shape. In order to characterize these global density distributions quantitatively, we fit each of them to a simple ellipsoidal profile:

$$\rho(\mathbf{x}) = \left[\frac{R_c^2}{R^2 + (z/q)^2} \right]^{\alpha/2}, \quad (15)$$

where $R_c (= 10 \text{ kpc})$ denotes the radius of the density normalization.

Figure 8 shows the reproduced density distribution along the Galactic plane (solid lines) and fitting curves (dashed lines). We find that all of the distributions have a discontinuity at $R \sim 8 \text{ kpc}$, and the density below this radius falls short of the

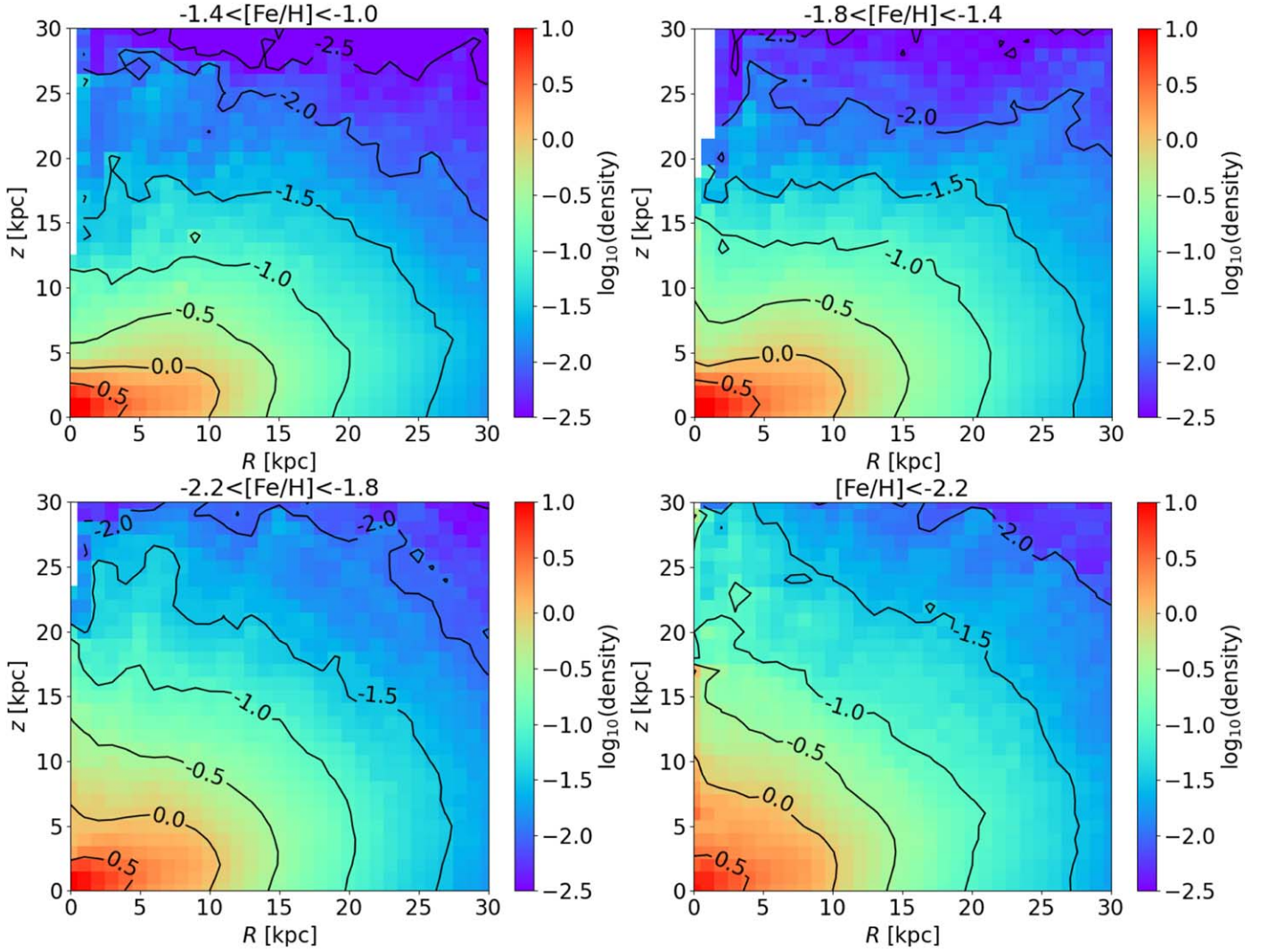


Figure 7. The constructed global density distribution calculated from the entire halo sample for the four different metallicity ranges: $-1.4 < [\text{Fe}/\text{H}] < -1.0$ (upper left); $-1.8 < [\text{Fe}/\text{H}] < -1.4$ (upper right); $-2.2 < [\text{Fe}/\text{H}] < -1.8$ (lower left); and $[\text{Fe}/\text{H}] < -2.2$ (lower right). The distribution is normalized at $(R, z) = (10 \text{ kpc}, 0)$.

fitting curves in all stellar metallicity ranges. The cause of this continuity is due to an observational bias (Sommer-Larsen & Zhen 1990): a star moving only within the region inside the position of the Sun, $r \sim 8 \text{ kpc}$, i.e., a star with apocentric radius $r_{\text{apo}} \lesssim 8 \text{ kpc}$, cannot reach the observable region near the Sun. Therefore, the observational data are devoid of these stars. This bias is also seen in Figure 3, where stars with $E < -1.5 \times 10^5 \text{ km}^2 \text{ s}^{-2}$, i.e., those orbiting inside the solar position, are lacking in the current local sample (see also Myeong et al. 2018b; Carollo & Chiba 2021). We thus avoid the innermost distribution $r < 8 \text{ kpc}$ for the following fittings.

We first determine the value of the slope α by the root-mean-square fitting of the radial distributions in Figure 8 to the power-law function $\rho \propto R^{-\alpha}$, i.e., the density distribution at $z=0$ in Equation (15). We obtain $\alpha = 3.2 - 3.4$ in the entire metallicity range. Specifically, the values of α in each metallicity range are $3.42^{+0.17}_{-0.07}$, $3.23^{+0.11}_{-0.08}$, $3.34^{+0.11}_{-0.11}$, and $3.42^{+0.09}_{-0.13}$, from the metal-rich to metal-poor ranges.

Next, we determine the value of an axial ratio, q , at each position r and metallicity range. Figure 9 shows the reproduced density distribution along $\theta = 0^\circ - 90^\circ$ at $r = 8, 15,$ and 25 kpc (solid lines). The dashed lines correspond to the ellipsoidal

fitting curves to these density distributions with a parameter q : while these lines are constant along θ in the case of a spherically symmetric case of $q = 1$, a smaller q , i.e., a more flattened axial ratio, leads to a more negative density gradient with increasing θ . We find that the stellar halo in a more metal-poor range has a rounder shape, and is more flattened in a metal-rich range. This result is in agreement with previous works before Gaia using much smaller numbers of sample stars (Chiba & Beers 2000; Carollo et al. 2007).

Figure 10 shows the radial distribution of q derived in this manner over $r = 8 - 30 \text{ kpc}$. We find that more metal-rich halo stars tend to have a smaller axial ratio q over the entire radii (except for a somewhat reversed trend in the ranges of $-1.8 < [\text{Fe}/\text{H}] < -1.0$ at $r > 20 \text{ kpc}$), and that the axial ratio of the most metal-poor halo ($[\text{Fe}/\text{H}] < -2.2$) is nearly 1 over the entire radii, i.e., having a nearly spherical shape.

It is worth remarking from Figures 7 and 9 that the actual shapes of the equidensity contours deviate from the ellipsoidal profiles in Equation (15): they have somewhat boxy or peanut-like shapes, so that the derived density distributions depicted in Figure 9 have a peak around $\theta \sim 15^\circ$, whereas simple ellipsoidal profiles should decrease monotonically with θ . We note that these

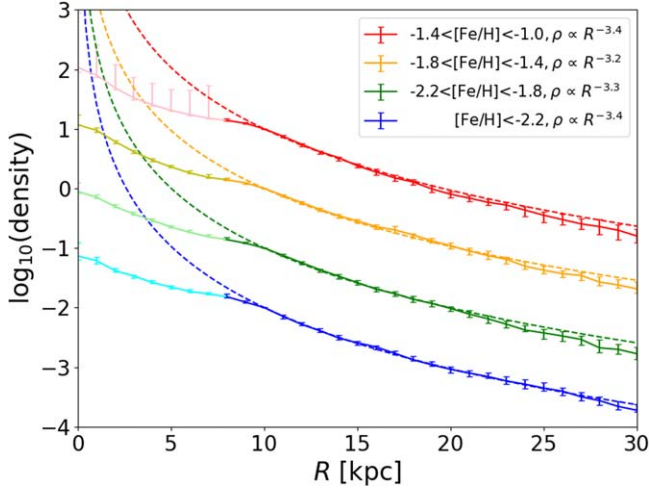


Figure 8. The density distribution along the Galactic plane, extracted from Figure 7. The solid lines show the reproduced distribution and the dashed lines present the fitting curves with a best-fit power-law slope, α . The colors of the lines correspond to the range of metallicity. The light colors indicate the region at $R < 8$ kpc, and are excluded from the fitting to the profile $\rho \propto R^{-\alpha}$. Each line is shifted vertically for the purpose of comparing between the different metallicity ranges. The error bars show the uncertainties propagating from the observational errors associated with the position on the sky, parallax, proper motion, and line-of-sight velocity. The error bars in the following figures also include all of these observational errors.

properties of the density shapes are related to the lack of halo stars with a small l_3 or small orbital angle θ_{\max} shown in Figures 4 and 6 (see Section 4.1.2). We quantify the degree of the derivation from ellipsoidal shapes by Δ , defined as

$$\Delta(r) = \sqrt{\frac{1}{N_\theta} \sum_{\theta_i} \frac{[\log_{10} \rho_{\text{obs}}(r, \theta_i) - \log_{10} \rho_{\text{fit}}(r, \theta_i)]^2}{\sigma_{\log_{10}[\rho_{\text{obs}}(r, \theta_i)]}^2}}, \quad (16)$$

where ρ_{obs} is the density calculated from Equation (10; the solid lines in Figure 9), ρ_{fit} is the fitted ellipsoid given in Equation (15; the dashed lines), and $N_\theta = 31$ is the number of bins for θ_i . Figure 11 shows the distributions of Δ having a sharp peak at $r = 10$ kpc, except for $[\text{Fe}/\text{H}] < -2.2$; the latter range shows spherical shapes with little deviation from the ellipsoidal distribution over a wide range of r . At $r > 10$ kpc, Δ is decreasing with r , where Δ is largest in $-1.8 < [\text{Fe}/\text{H}] < -1.4$.

These behaviors in Figure 11 suggest that some substructures that perturb the ellipsoidal profile exist at around $r = 10$ kpc in $[\text{Fe}/\text{H}] > -2.2$ and $r > 10$ kpc in $-1.8 < [\text{Fe}/\text{H}] < -1.4$. This may include the presence of the metal-weak thick disk (MWTd; e.g., Beers et al. 2002; Carollo et al. 2019) at $r < 10$ kpc and/or the presence of the Monoceros Stream (Newberg et al. 2002; Ibata et al. 2003; Yanny et al. 2003). Alternatively, a large Δ may suggest that the shape of the stellar halo is intrinsically boxy or peanut-like, rather than spheroidal. We discuss the origin of this characteristic shape of the halo in more detail in 4.1.2.

3.1.2. Velocity Distribution

Next, using Equation (13), we obtain the global rotational velocity distribution, $\langle v_\phi \rangle$. The results for the relatively metal-rich ranges are shown in Figure 12. We find that the stars in $-1.2 < [\text{Fe}/\text{H}] < -1.0$ have a relatively large rotation, whose maximum is over 100 km s^{-1} . This disk-like structure is local, $R \lesssim 10$ kpc and $z \lesssim 3$ kpc, and decays with lowering stellar

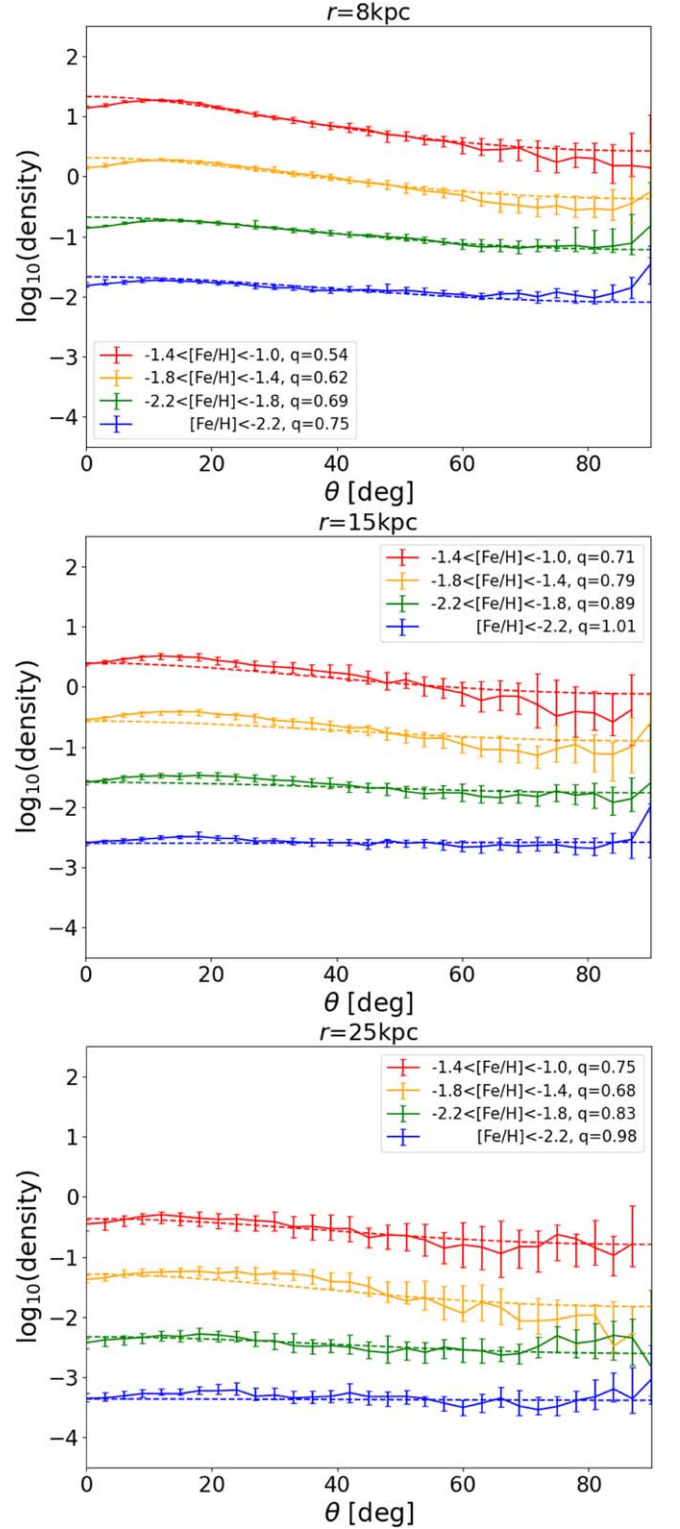


Figure 9. The density distribution along $\theta = 0^\circ - 90^\circ$ at $r = 8, 15,$ and 25 kpc (the solid lines) and the fitted curves with the ellipsoidal profile of Equation (15; the dashed lines) for each metallicity range. Each curve at a different r is shifted vertically for the comparison between the different metallicity ranges.

metallicity. It is consistent with the properties of the MWTd. Outside the disk-like region, the velocity field is almost 0, with no significant prograde and retrograde rotation.

Figure 13 shows the rotational velocity distribution along the Galactic plane $z = 0$. The mean rotational velocity in

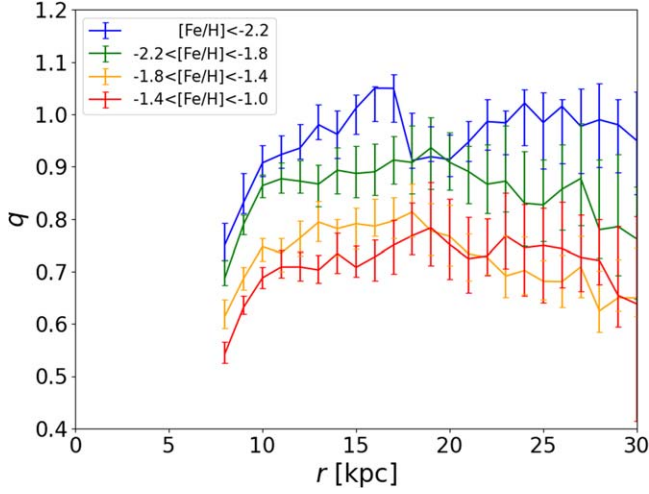


Figure 10. The axial ratio q of the ellipsoidal profile of Equation (15) as a function of the Galactocentric distance r for each metallicity.

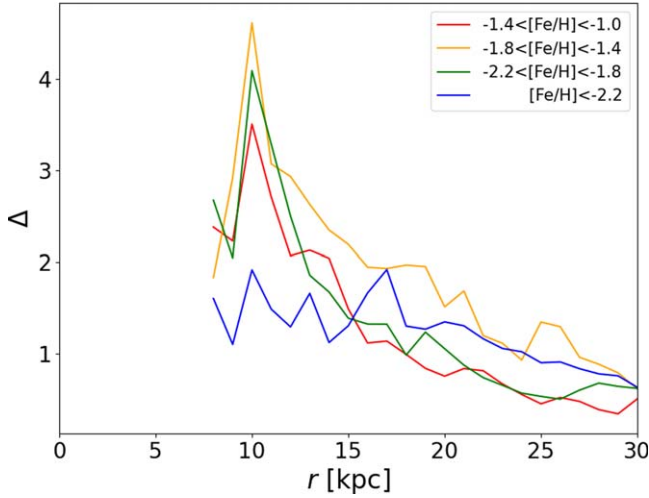


Figure 11. The degree of derivation, Δ , defined in Equation (16), between the reproduced density distribution of Equation (10) and the fitting ellipsoidal profile of Equation (15), normalized by each uncertainty.

$-1.2 < [\text{Fe}/\text{H}] < -1.0$ is more than twice those of the other metallicity ranges at $8 < R < 15$ kpc. On the other hand, over $R > 20$ kpc, $\langle v_\phi \rangle$ is almost zero in all metallicity ranges.

Note that Figure 13 shows the mixture distribution of the stellar disk and the stellar halo. Carollo et al. (2019) showed that the rotational velocity of the MWTD reaches $\sim 150 \text{ km s}^{-1}$, while Figure 13 shows that the maximum velocity is $\sim 110 \text{ km s}^{-1}$. This difference is due to the contamination of the halo stars, which move relatively randomly with less rotation. Thus, Figure 13 underestimates the velocity distribution of the pure MWTD. For the same reason, we do not claim that the metallicity of the MWTD is only over $[\text{Fe}/\text{H}] > -1.2$.

Additionally, Figures 12 and 13 show that for the metal-poor stars, especially in $[\text{Fe}/\text{H}] < -2.2$, the velocity field in the outer region, $R > 15 - 20$ kpc, is slightly but systematically negative below zero about 1σ uncertainty, but this feature is not thought to be real for the MW's stellar disk. This rotational property for very metal-poor stars in the outer region is in agreement with the retrograde rotation of the

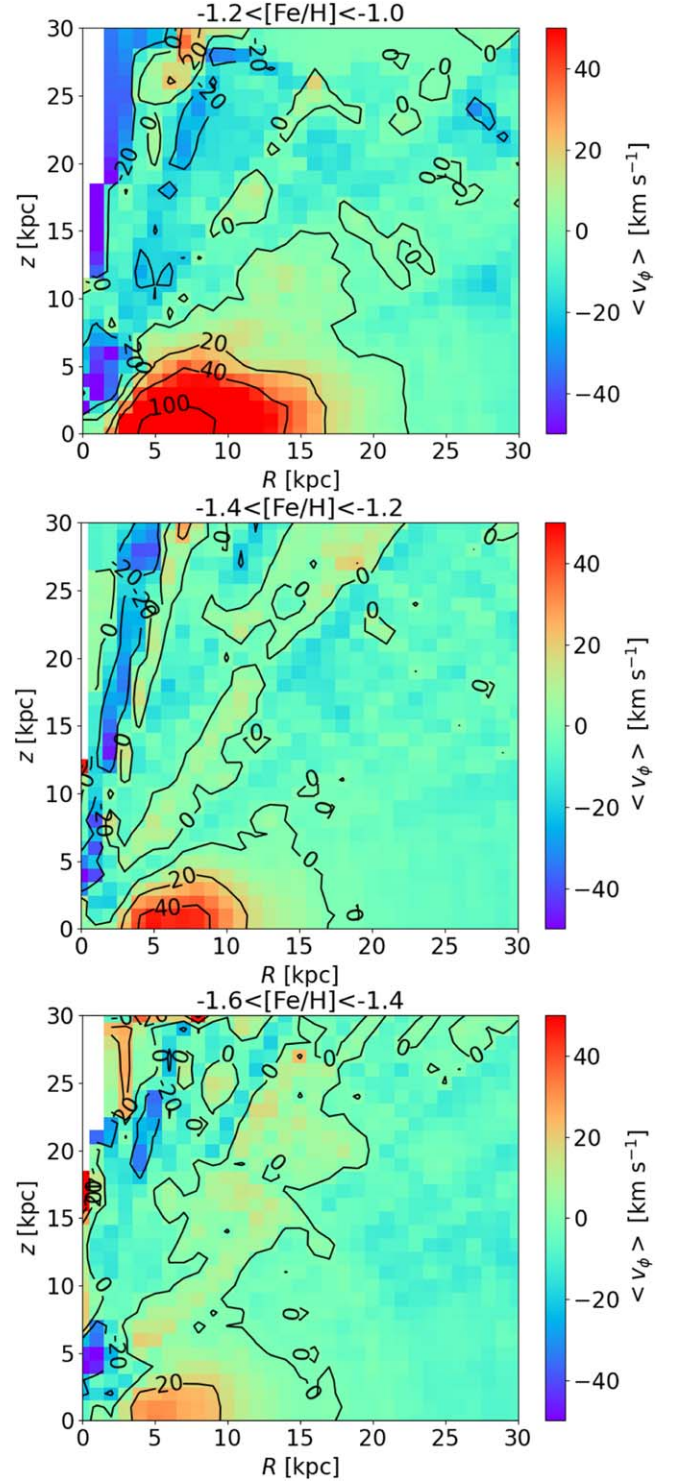


Figure 12. The global distribution of $\langle v_\phi \rangle$, defined in Equations (13) and (14), for the halo samples with $-1.2 < [\text{Fe}/\text{H}] < -1.0$ (top), $-1.4 < [\text{Fe}/\text{H}] < -1.2$ (middle), and $-1.6 < [\text{Fe}/\text{H}] < -1.4$ (bottom). As is clear, there exists a region with disk-like kinematics (as realized by the red color) corresponding to the MWTD.

outer-halo sample stars (e.g., Carollo et al. 2010). While the samples of previous research show a significant retrograde rotation at the solar position, the rotational value at $R \sim 30$ kpc in this work is reduced at the currently derived one under the angular-momentum conservation.

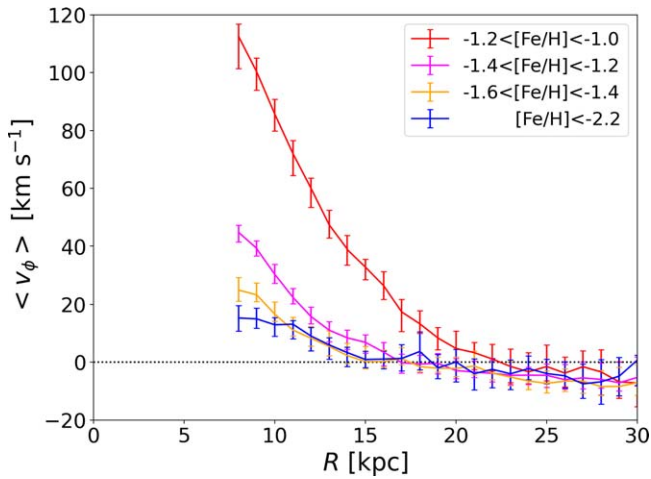


Figure 13. The mean rotational velocity along the Galactic plane for each metallicity range. The dotted line indicates the zero velocity.

3.2. The GSE-like Subsample

We carry out the same analysis for the subsample stars showing GSE-like kinematics. The derived density distributions for this subsample are shown in Figure 14, for the different metallicity ranges, which are the same as in Figure 7. We fit this distribution to the ellipsoidal profile given in Equation (15).

Figure 15 shows the density distribution along the Galactic plane (the solid lines), from which we can determine the slope α given in Equation (15) for the ellipsoidal profile (the dashed lines). We note that in Figure 15 there are discontinuities at $R \sim 8$ kpc, i.e., at the same position in Figure 8. Since these discontinuities can be due to the observational bias, as is the case in the entire halo sample, we do not use these inner radii to determine the value of α .

The determined values of α are $2.94^{+0.16}_{-0.05}$, $2.89^{+0.13}_{-0.00}$, $3.28^{+0.15}_{-0.03}$, and $3.47^{+0.24}_{-0.08}$, respectively, from the metal-rich to metal-poor ranges. Compared with the case of the entire halo sample, the slopes in the relatively metal-rich range, $[\text{Fe}/\text{H}] > -1.8$, are systematically smaller, and those in the more metal-poor range, $[\text{Fe}/\text{H}] < -1.8$, are almost the same. This result is consistent with the fact that GSE appears only in a relatively metal-rich range (Belokurov et al. 2018). The small α means that the density distribution of the GSE-like subsample decreases with Galactocentric distance more slowly than the general stellar halo.

It is worth noting in Figure 15 that the derived density distribution falls short of a single power-law distribution at around $R = 20$ kpc in the relatively metal-rich range, $[\text{Fe}/\text{H}] > -1.8$. This feature does not appear in the entire halo sample shown in Figure 8. We note that we do not artificially remove the region at $R > 20$ kpc when we fit the global distribution and determine α . Thus, we conclude that the density distribution of the GSE-like sample shows a drop at around 20 kpc, which may correspond to GSE’s radial boundary (see Section 4.2).

To clarify that the drops are real properties of the GSE-like subsample, we calculate the value indicating the deviation of the reconstructed density distribution from the ellipsoidal profile, defined as

$$\Delta_\theta^2(r) = \frac{[\log_{10} \rho_{\text{obs}}(r, \theta) - \log_{10} \rho_{\text{fit}}(r, \theta)]^2}{\sigma_{\log_{10}[\rho_{\text{obs}}(r, \theta)]}^2}. \quad (17)$$

This is the same as the factors of the sum in Equation (16). We calculate both $\Delta_{\theta=0^\circ}(r)$ for the entire halo sample and the GSE-like subsample, and compare them in Figure 16. We find that $\Delta_{\theta=0^\circ}(r)$ of the GSE-like subsample in $-1.8 < [\text{Fe}/\text{H}] < -1.0$ gets remarkably large values at $10 \lesssim r \lesssim 15$ kpc and $r \gtrsim 20$ kpc. This figure also suggests that the GSE-like subsample in the $-1.8 < [\text{Fe}/\text{H}] < -1.0$ range does not follow the power-law profile at $r \gtrsim 20$ kpc, so this is GSE’s characteristic length. On the other hand, the reason of the large $\Delta_\theta(r)$ at $10 \lesssim r \lesssim 15$ kpc is due to the nonellipsoidal shape, like a boxy or peanut-like shape, shown in Figure 11.

Next, we determine the value of the axial ratio q for this subsample. The result is shown in Figure 17, compared with the case of the entire halo sample. We find that in the relatively metal-rich range $[\text{Fe}/\text{H}] > -1.8$, the axial ratios of the GSE-like subsample are systematically larger than those of the general stellar halo at $r < 15$ kpc, whereas the q of the GSE-like subsample is smaller beyond $r \sim 20$ kpc. This is consistent with Figure 15, implying the presence of the radial boundary of the GSE-like members at 20 kpc. On the other hand, the axial ratios for the more metal-poor ranges are larger than or almost the same compared with the ones of the general stellar halo. Their larger axial ratios may come from the dynamical selection $L_z \sim 0$.

Finally, we remark on the $\langle v_\phi \rangle$ distribution of this GSE-like sample. We also find no remarkable structures like the MWTD even in the metal-rich ranges, because of the preselection of this sample with L_z around 0.

4. Discussion

The derived global structures of the current halo sample based on the superposition of their orbits suggest several implications for the formation and evolution histories of the MW’s stellar halo. We discuss here what insights are inferred from the current analysis in comparison with recent numerical simulations for the formation of stellar halos.

4.1. Global Halo Structure from the Entire Sample

4.1.1. Implications from Axial Ratios and Radial Profiles

As clearly shown in Figure 10, the global shapes of the relatively metal-rich stellar halos in the range of $[\text{Fe}/\text{H}] > -1.8$ have smaller axial ratios q , i.e., are more flattened, than the more metal-poor halos with $[\text{Fe}/\text{H}] < -1.8$ over all radii. Also, at radii below 18 kpc, we find that a more metal-rich halo shows a more flattened shape for all of the metallicity ranges below $[\text{Fe}/\text{H}] = -1$.

The flattened structures in the relatively metal-rich ranges may, at least partly, be affected by the presence of the MWTD at $[\text{Fe}/\text{H}] < -1$. The disk-like motion of the MWTD is appreciable in the $\langle v_\phi \rangle$ distribution of the $-1.2 < [\text{Fe}/\text{H}] < -1.0$ range (Figures 12 and 13), with radial and vertical sizes of ~ 14 kpc and ~ 4 kpc, respectively. If we adopt a condition, $\langle v_\phi \rangle / \sigma_\phi > 1$, with $\sigma_\phi = 50 \text{ km s}^{-1}$ as a typical velocity dispersion of the thick disk in ϕ direction (Chiba & Beers 2000), these figures also show that such a disk-like motion quickly becomes weak in $-1.4 < [\text{Fe}/\text{H}] < -1.2$, where $\langle v_\phi \rangle / \sigma_\phi$ is smaller than 1 at all radii, so the effect of the MWTD may be sufficiently weak at $[\text{Fe}/\text{H}]$ between -1.4 and -1.2 . The fact that the derived relatively metal-rich halo sample shows a flattened shape over the regions beyond where

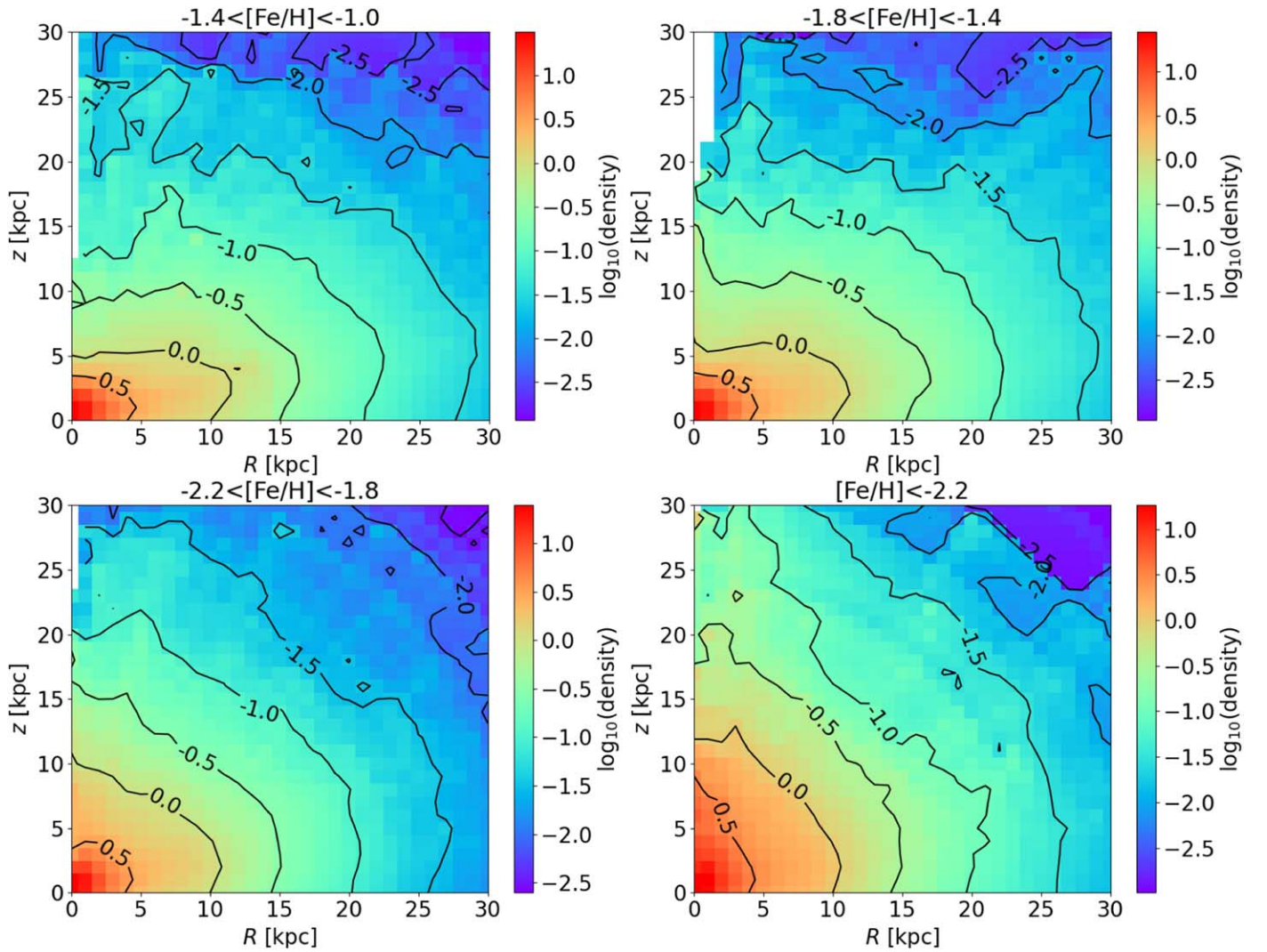


Figure 14. The contour of the global density distribution of the GSE-like subsample. The normalization and metallicity ranges are the same as in Figure 7.

this MWTD-like feature permeates suggests that this flattened structure is a real halo structure. These flattened parts of the halo may correspond to the in situ halo, in which stars have been formed inside a main parent halo.

The formation of this flattened halo part may be explained within the framework of the cold dark matter (CDM) model (White & Rees 1978; Bekki & Chiba 2000): a flattened structure of a relatively metal-rich halo was formed by dissipative merging of a few massive clumps at an early stage of the MW’s evolution. Alternatively, this flattened structure can be a dynamically heated, preexisting disk, driven by falling satellites (e.g., Benson et al. 2004; Purcell et al. 2010; McCarthy et al. 2012; Tissera et al. 2013; Cooper et al. 2015).

On the contrary, the more metal-poor halos have a structure closer to a sphere, and this characteristic suggests that it is the ex situ halo component. The presence of this metal-poor, spherical halo is consistent with the MW’s formation scenario under the CDM model: the outer halo was formed by the later accretion of small clumps resembling metal-poor dwarf spheriodals, which are stripped by tidal force from the MW’s dark halo (Bekki & Chiba 2001; Carollo et al. 2007).

Recent numerical simulations based on CDM models provide similar chemodynamical properties of stellar halos to those

reported here. Monachesi et al. (2019) simulated the formation process of MW-like stellar halos with accretions of stars. The simulation showed that the axial ratios of the halos are typically 0.6 to 0.9 at $R = 20\text{--}40$ kpc. This simulated range is consistent with our result shown in Figure 10. The simulation also showed that the shapes of MW-like stellar halos can be prolate in outer regions, where the ex situ component dominates. Our result of $[\text{Fe}/\text{H}] < -2.2$ range has the same shape, so it is considered that the ex situ component is dominant in this metallicity range.

Regarding the radial density slope, α , the derived values in this work are almost the same, 3.2–3.4, in the different metallicity ranges, though there may exist varieties in the formation processes. Rodriguez-Gomez et al. (2016) and Monachesi et al. (2019) showed that the accreted halo components have a shallower density slope with $\alpha < 3.0$, in the radius range $15 < r < 100$ kpc, than the in situ components. On the other hand, in the range $8 < r < 30$ kpc, with which the current work is concerned, the ex situ halo should be less dominant than in the range of $15 < r < 100$ kpc. Thus, the values of α may not be strongly affected by the later accretion process of small clumps, and this work obtains almost the same values of α for the different metallicity ranges.

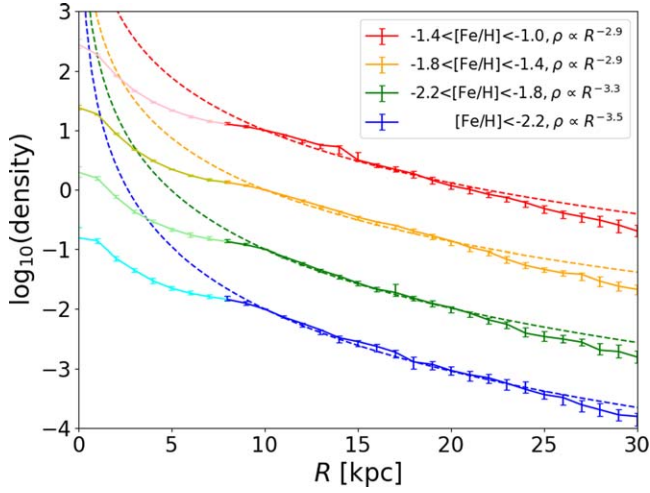


Figure 15. The distribution of the GSE-like subsample along the Galactic plane (the solid lines) and their fitting curves with a power law (the dashed lines), to be compared with Figure 8 for the entire halo sample. This comparison indicates that the density distribution of the GSE-like subsample shows a noticeable drop at $R \sim 20$ kpc in the metallicity range of $[\text{Fe}/\text{H}] > -1.8$.

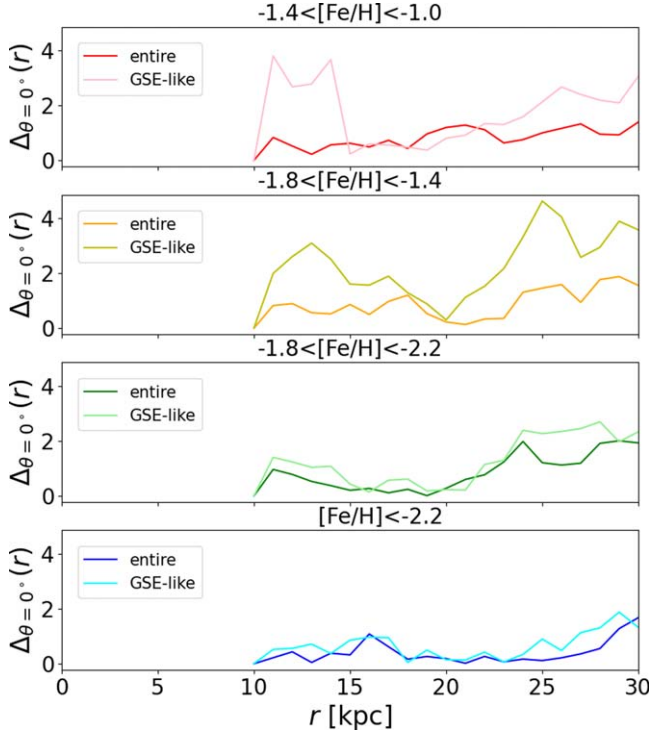


Figure 16. The degree of deviation of the reconstructed density distribution from the ellipsoidal fitting profile along the Galactic plane, $\Delta_{\theta=0^\circ}(r)$, defined by Equation (17).

4.1.2. Implications from the Boxy/Peanut-shape Configuration

Here we discuss the origin of the nonellipsoidal profile peaked at around $r \sim 10$ kpc, as shown in Figure 7. We note that the presence of the MWTD is insufficient to explain this feature, because the nonellipsoidal structure is most prominent within $-1.8 < [\text{Fe}/\text{H}] < -1.4$, whereas the MWTD dominates in $-1.4 < [\text{Fe}/\text{H}] < -1.0$ (Figures 12 and 13). We consider two possibilities for explaining this feature.

First, the intrinsic structure of the inner part of the MW's stellar halo forms a boxy/peanut-like shape rather than the

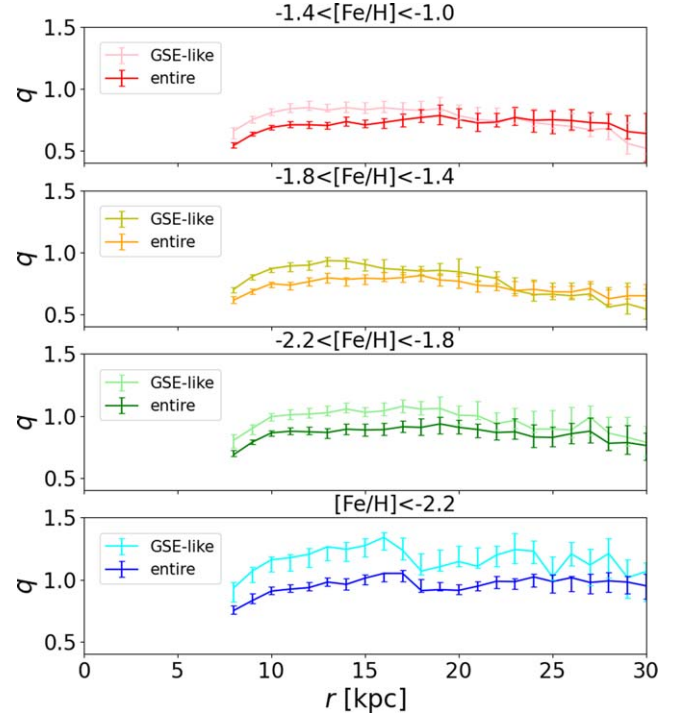


Figure 17. The axial ratios q of the GSE-like subsample compared with those of the entire halo sample as a function of the Galactocentric distance r for each metallicity range.

ellipsoidal shape at $r < 20$ kpc. Carollo et al. (2007, 2010) showed that the inner halo component is dominant up to $r = 10 - 15$ kpc, and the outer halo is dominant at $r > 20$ kpc. These two regions, $r = 10 - 15$ kpc and $r > 20$ kpc, correspond to those where the current deviation measure from an ellipsoidal shape, Δ , shows a peak and is relatively small, respectively.

Figure 9 shows that the density distributions along $r = 8$ and 15 kpc are curved upward at around $\theta \sim 15^\circ$ and downward over $\theta > 60^\circ$. In fact, the density deficiency at large θ also appeared in the results of Sommer-Larsen & Zhen (1990), Chiba & Beers (2000), and Carollo et al. (2007). It was interpreted due to the observational bias: there is a small probability that such stars orbiting at large θ are represented in the solar neighborhood, and this effect may have been nonnegligible in previous works using only the small number of sample stars available before Gaia. However, our reconstruction using the more numerous stars cataloged in Gaia leads to a similar shape of the density distribution of the MW's stellar halo. There are indeed no discontinuities in the observational inclination distribution shown in Figure 6. Thus, we regard the boxy/peanut-shaped structure as a real feature, not biased.

It is also worth remarking in Figure 6 that there is a sharp drop in the number of orbits at $\theta_{\text{max}} < 10^\circ$. Carollo & Chiba (2021) showed that the lack of these low- θ (or low- I_3) stars is not artificial: if stars with small orbital inclinations really exist in the MW, such stars surely pass by the solar neighborhood and thus can be included in the current local sample. This fact means that since such low- θ stars possess highly eccentric, radial orbits, they can surely be identified, if they exist, in the current survey volume. As a result, the lack of such stars near the Galactic plane leads to the reconstructed global density distribution having a boxy shape.

Second, the nonellipsoidal structure of the halo may reflect the Monoceros Stream (Newberg et al. 2002; Ibata et al. 2003; Yanny et al. 2003). This stream feature is a ring-shaped overdensity with a heliocentric radius of 6 kpc in the south and 9 kpc in the north (Morganson et al. 2016), and a height of $3 < z < 4$ kpc (Ivezić et al. 2008). These spatial distributions generally agree with our results that the density contours in Figure 7 are curved upward to a similar vertical range, and the nonellipsoidal structure, as shown in Figure 11, is dominant over the similar Galactocentric distance.

However, Ivezić et al. (2008) and Morganson et al. (2016) showed that the Monoceros Stream is centered at $[\text{Fe}/\text{H}] = -0.95$ and spreads between $-1.1 < [\text{Fe}/\text{H}] < -0.7$. This metallicity is quite different from the range where the nonellipsoidal structure dominates in Figure 11, $-1.8 < [\text{Fe}/\text{H}] < -1.4$. This suggests that the nonellipsoidal structure of the stellar halo obtained here is not due to the Monoceros Stream.

We thus conclude that the nonellipsoidal structure of the stellar halo, which is mainly revealed in the inner parts of the halo, is a physically real feature, and this shape of the stellar halo is considered to reflect the MW’s merger history. It is known that a merger between early-type gas-poor galaxies with the same masses (a dry and major merger) forms a boxy-shaped elliptical galaxy (Bell et al. 2006; Cox et al. 2006; Naab et al. 2006). Even including gas in the merging process, although gas dissipates into the equatorial plane and forms more metal-rich stars with disk-like kinematics, the preexisting stars in the progenitor satellites can end up with a boxy structure after merging, consisting of 3D box orbits. Also, the dynamical heating of this formed disk through the later merging of satellites is another source of halo stars, where the heating process can be more effective in the outer disk regions due to weaker vertical gravitational force, so that the heated debris would have a peanut-shaped structure, like the edge-on view of long-lived bars (Athanasoula 2005). Indeed, the simulation works under CDM scenarios show some boxy/peanut-shaped stellar halos (e.g., Bullock & Johnston 2005; Cooper et al. 2010; Monachesi et al. 2019). Further theoretical works will be needed to quantify this nonellipsoidal structure of the simulated halos and clarify what merging histories of progenitor galaxies are associated with this characteristic structure.

4.1.3. On the Discontinuities from the Observational Bias

We have mentioned that the reproduced density distribution has remarkable discontinuities at $R \sim 8$ kpc (see Figures 8 and 15). These discontinuities are caused by the observational bias that stars orbiting only in the inner region of $R \lesssim 8$ kpc never reach the observable region near the Sun, and are not contained in the currently adopted stellar catalog. However, in principle, it is also conceivable that another discontinuity may appear, caused by stars staying far from the Sun, but we do not find such discontinuities. This subsection explains the properties of the observational bias caused by stars staying inside and outside the locally observable region.

In the following, “the inner region” is defined as $|z| < (R - R_\odot)\tan 165^\circ$ and “the outer region” is $|z| < (R - R_\odot)\tan 15^\circ$, which, respectively, are the X-shape vacant regions in Figure 1. Stars staying in either of these regions are never included in the observational sample.

Figure 18 shows the E - I_3 space distribution, similar to Figure 4, but the color of the points indicates the range of $|L_z|$. The shaded

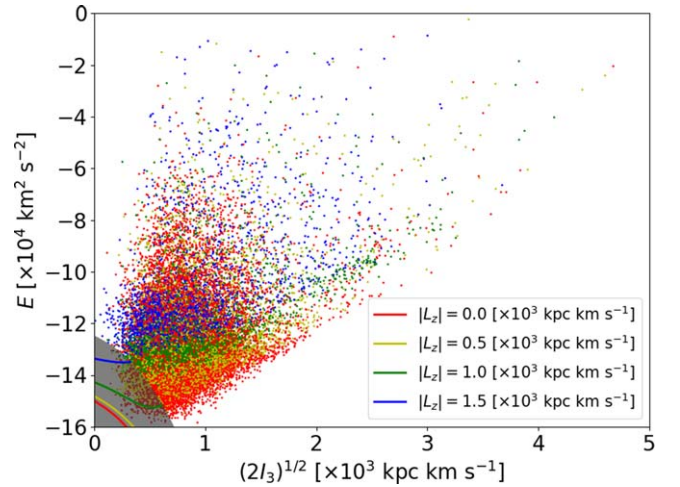


Figure 18. The distribution of the sample stars in the phase space ($\sqrt{2I_3}$, E). The color of the points indicates the vertical angular momentum $|L_z|$ of the stars —red: $0.0 < |L_z| < 0.5$; yellow: $0.5 < |L_z| < 1.0$; green: $1.0 < |L_z| < 1.5$; and blue: $|L_z| > 1.5$ (in units of $L_z: \times 10^3$ kpc km s $^{-1}$). The shaded region is the area where the stars stay only in “the inner region” relative to the survey volume, depending on the values of $|L_z|$ depicted with the color-coded lines: such stars having $|L_z|$ larger than a specific value are located below the corresponding color-coded line within the shaded region.

region indicates the area where stars staying in the inner region are located, depending on their $|L_z|$. For example, stars staying in the inner region with $|L_z| > 1.0 \times 10^3$ kpc km s $^{-1}$ are located in the shaded region below the green line. In other words, the stars shown with green and blue points (the observed stars with $|L_z| > 1.0 \times 10^3$ kpc km s $^{-1}$) cannot be located in the shaded region below the green line due to the bias. It is clear that the shaded region in Figure 18 demonstrates the observational bias in the inner region.

Figure 19 also shows the E - I_3 space distribution, but the shaded region indicates the area where the stars stay only in the outer region. In this case, for example, red-pointed stars (with $|L_z| > 2.0 \times 10^3$ kpc km s $^{-1}$) cannot be located in the shaded region below the red line; this prohibited region is so small. For another example, stars with $|L_z| > 7.0 \times 10^3$ kpc km s $^{-1}$ are greatly constrained, such that they cannot be located in the wide shaded region below the blue line, but such stars with high $|L_z|$ do not exist at least within $R \sim 35$ kpc, provided that the circular rotation velocity there remains about 200 km s $^{-1}$ (see Figures 2 and 3)). Additionally, the black points ($|L_z| < 2.0 \times 10^3$ kpc km s $^{-1}$; 96% of the sample) are not limited to the E - I_3 plane, which means that they cannot stay in the outer region. This suggests that stars staying only in the outer region are few, so the corresponding discontinuity is not expected to appear.

The recent study of Carollo & Chiba (2021) supports the current argument. It showed that the $\sqrt{2I_3}$ distribution quickly damps at around $\sqrt{2I_3} \sim 0.5 \times 10^3$ kpc km s $^{-1}$. Stars staying in the outer region need to have a small inclination θ_0 . Figure 5 shows that θ_0 strongly correlates with I_3 . Thus, the damping of the $\sqrt{2I_3}$ distribution suggests that the stars staying in the outer region are very few. On the other hand, the stars staying in the inner region need to have low E . In Figure 3, the dotted line descends beyond the frame around $|L_z| \sim 0 - 1.0 \times 10^3$ kpc km s $^{-1}$, but the data points do not follow the lower-limit lines. The gap between the dotted line and the fiducial points suggests that there are many inner stars not captured by

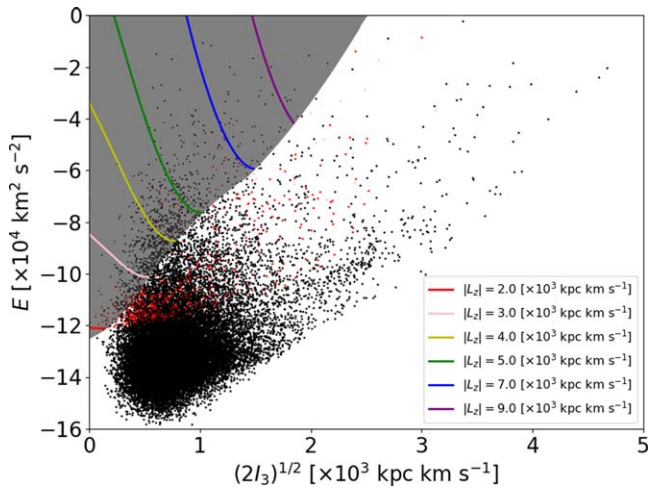


Figure 19. The phase-space distribution of the sample stars as in Figure 18, but with the colors of the points corresponding to different ranges for $|L_z|$ —black: $0.0 < |L_z| < 2.0$; red: $2.0 < |L_z| < 3.0$; pink: $3.0 < |L_z| < 4.0$; and yellow: $|L_z| > 4.0$ (in units of L_z ; $\times 10^3$ kpc km s^{-1}). The shaded region is the area where the stars stay only in “the outer region” relative to the survey volume, depending on the values of $|L_z|$ depicted with the color-coded lines: such stars having $|L_z|$ larger than a specific value are located below the corresponding color-coded line within the shaded region.

observations. Therefore, the discontinuities at around $R \sim 8$ kpc appear, while there are no discontinuities in the outer region.

4.2. Global Structure from the GSE-like Subsample

As shown in Figure 15, the distributions of the GSE-like subsample in $-1.8 < [\text{Fe}/\text{H}] < -1.0$ fall short of a single power-law profile at $R \sim 20$ kpc on the Galactic plane. This metallicity range is just consistent with the reported metallicities for the likely GSE member stars (Belokurov et al. 2018; Koppelman et al. 2019). By combining this with the result in Figure 16, we regard 20 kpc as GSE’s likely radial scale.

The result that GSE’s scale is 20 kpc is consistent with some previous works. Naidu et al. (2020) showed the occupancy fraction of each substructure as a function of position, based on the observations of the H3 survey, and revealed that GSE’s fraction peaks at $r \sim 20$ kpc and rapidly declines with increasing r . Deason et al. (2018) found that the sausage-like structure in the stellar halo has its apocenter at 25–30 kpc. Lancaster et al. (2019) also indicated that GSE’s density rapidly decreases at 20 kpc.

This scale is considered to indicate the position of the apocenter of GSE’s progenitor. Because it is thought that GSE is a tracer of a merger event between the MW and a large dwarf galaxy about 10 Gyr ago, the radius 20 kpc should be the characteristic scale of the event. That “characteristic scale” is typically expected to indicate the apocenter of the merged galaxy (Deason et al. 2018; Lancaster et al. 2019).

Furthermore, the distance of 20 kpc is consistent with the end where the inner halo is dominant (Carollo et al. 2007, 2010), so our result suggests that GSE is the dominant substructure within the inner halo. This inference is supported by the behavior in $r = 10 - 15$ kpc of the GSE-like sample. We have mentioned that the large values of $\Delta(r)$ might be the feature of the inner halo (Section 4.1.2), and Figure 16 shows that $\Delta_{\theta=0^\circ}(r)$ in $r = 10 - 15$ kpc and $-1.8 < [\text{Fe}/\text{H}] < -1.0$ of the GSE-like sample is much larger than that of the entire halo

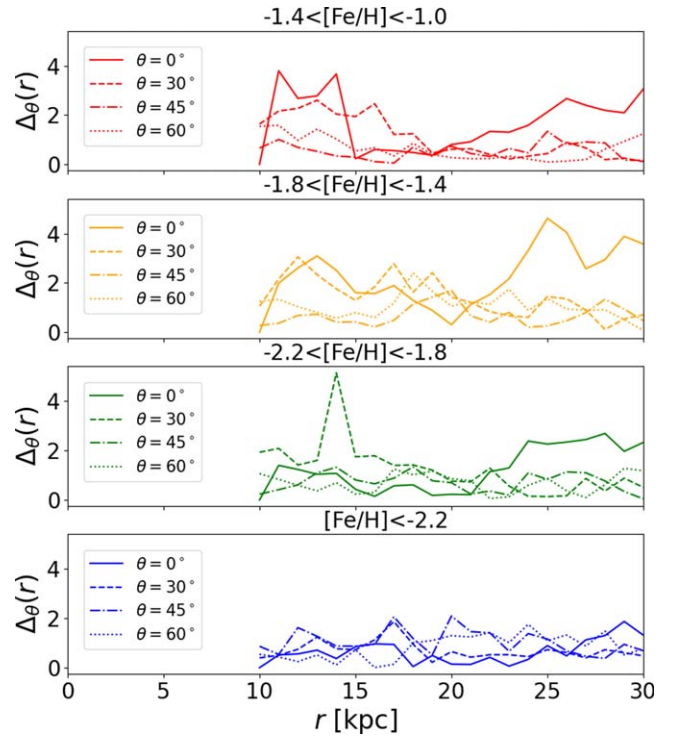


Figure 20. The degree of the deviation $\Delta_\theta(r)$ of the GSE-like sample along $\theta = 0^\circ, 30^\circ, 45^\circ$, and 60° , which correspond to the solid, dashed, dashed-dotted, and dotted lines, respectively.

sample. Namely, the GSE-like sample reflects the basic properties of the inner halo significantly.

We also attempt to find the characteristic inclination θ of the GSE-like sample. Figure 20 shows the deviation measure $\Delta_\theta(r)$ of the GSE-like sample for various θ . It shows that three lines, except for $\theta = 0^\circ$, are similar and have no remarkable difference for each metallicity range. Exceptionally, the $\theta = 30^\circ$ line of $-2.2 < [\text{Fe}/\text{H}] < -1.8$ has a sharp peak at $R \sim 14$ kpc, but this is likely to be an outlier. Thus, GSE’s characteristic inclination is not available here.

Next, we have shown that the slope α of the GSE-like subsample in $-1.8 < [\text{Fe}/\text{H}] < -1.0$ is 2.9, being systematically smaller than the slopes of the general halo, $\alpha = 3.2 - 3.4$. On the other hand, in the more metal-poor ranges $[\text{Fe}/\text{H}] < -1.8$, the values of α are almost the same for both samples. As shown in Section 4.1.1, it is known that accreted halo components have a smaller α with $\alpha < 3.0$ (Rodríguez-Gomez et al. 2016; Monachesi et al. 2019). Thus, the smaller α of the GSE-like subsample in our work is consistent with its origin.

Additionally, Figure 17 shows that the axial ratios of the GSE-like subsample in $-1.8 < [\text{Fe}/\text{H}] < -1.0$ are systematically larger than the general stellar halo within $r \lesssim 20$ kpc, suggesting that GSE’s shape is closer to a sphere than the general halo. This property of GSE, which is a merging origin, was also suggested in the simulation work by Monachesi et al. (2019). It showed that a stellar halo that recently experienced the accretion of a satellite forms a more spherical shape than a general halo.

4.3. The Completeness of the Observational Data

This work analyzes the global distribution of the MW’s stellar halo by using local observational data. There might be

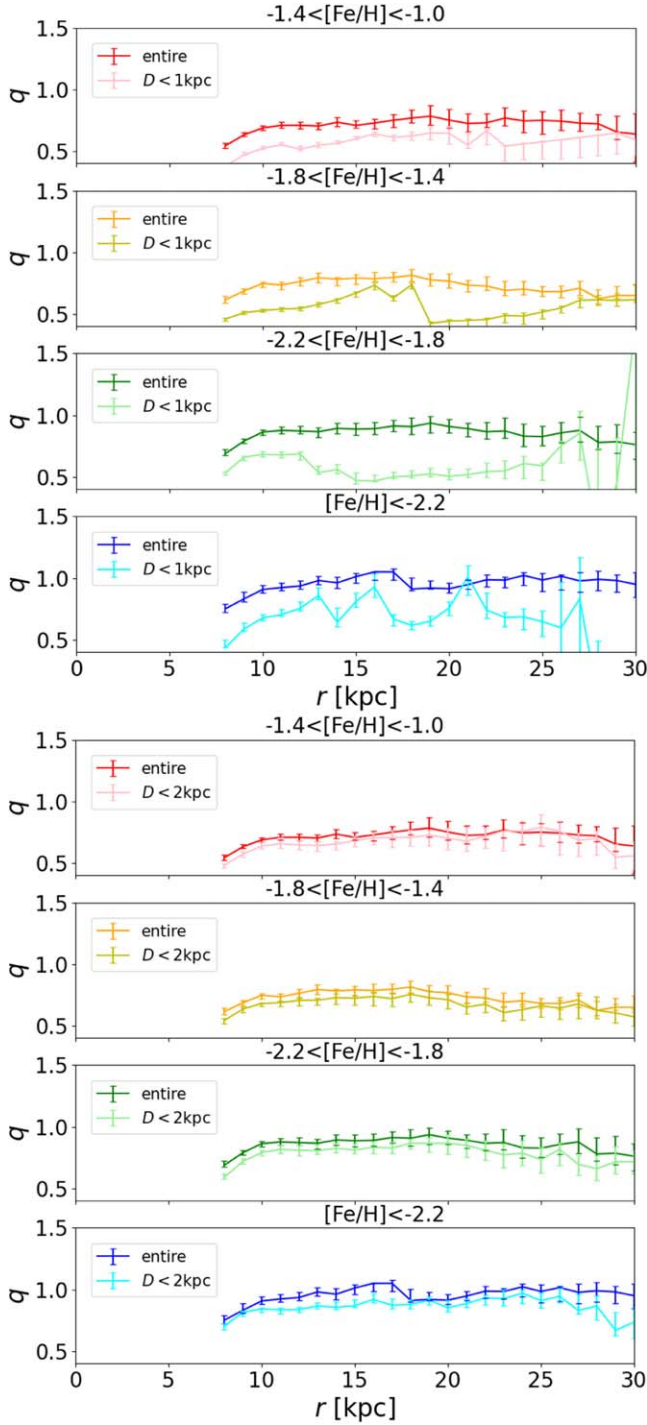


Figure 21. The results for the axial ratio of the subsamples of $D < 1$ kpc (the upper panel) and $D < 2$ kpc (the lower panel), compared with the main sample (the dark-colored lines, which are the same as in Figure 10).

some concerns about the effect of the completeness of the result. We carry out some additional analysis below to get insights into this issue.

We create two other subsamples, whose additional selection conditions are that the heliocentric distance, D , is smaller than 1 kpc and 2 kpc, respectively. We carry out the same analysis for these subsamples.

The axial ratio of these subsamples is shown in Figure 21 as the representative result. In the case of $D < 1$ kpc, the reconstructed distribution is very bumpy, with large uncertainty

(the upper panel of Figure 21), so this result has poor reliability. Two reasons for the poor reliability are considered. The first reason is that the $D < 1$ kpc sample has too few stars (1895 stars; 7.6% of the main sample) to reproduce the global distribution. The second is that the region within 1 kpc from the Sun is too small to represent a global distribution. In any case, this result has insufficient completeness.

On the other hand, for the $D < 2$ kpc subsample, we obtain a result that is almost the same as the main result (the lower panel of Figure 21). It is suggested that the completeness of the $D < 2$ kpc subsample is sufficient to reproduce the global distribution up to ~ 30 kpc. Therefore, this suggests that our main result, using stellar $D \lesssim 4$ kpc, is insensitive to the sample's completeness.

5. Conclusion

We have constructed and analyzed the global distribution of the MW's stellar halo using the Gaia EDR3 catalog combined with the SDSS DR16 SEGUE catalog. For this purpose, we adopt the method developed by Sommer-Larsen & Zhen (1990), following the strategy of May & Binney (1986), of reconstructing the global halo based on the superposition of the stars' orbits. We calculate the orbital density of each star and assign a proper weight to it through a maximum likelihood approach. We then sum up all of the orbital densities with these weights, and derive the global stellar distribution from the observational sample stars currently located within a local volume near the Sun.

We have found that the more metal-rich halo stars show more flattened distributions, as have been derived in previous studies using much smaller numbers of sample stars (e.g., Carollo et al. 2007). In the metal-rich range of $-1.4 < [\text{Fe}/\text{H}] < -1.0$, we have identified, through the reconstruction of global rotational velocities, $\langle v_\phi \rangle$, the presence of the MWTD at $z < 4$ kpc and $R < 15$ kpc. The detailed configuration of the global halo structures in the relatively metal-rich ranges of $[\text{Fe}/\text{H}] > -1.8$ is found to have a boxy/peanut shape rather than a simple ellipsoidal shape, and this may reflect a past merging event. On the other hand, in the most metal-poor range of $[\text{Fe}/\text{H}] < -2.2$, the halo structure is close to a spherical shape.

We have selected a subsample of GSE-like stars with $E > -150,000 \text{ km}^2 \text{ s}^{-2}$ and $-500 < L_z < 500 \text{ kpc km s}^{-1}$. In contrast to the entire halo sample, the global density profile of these GSE-like stars shows a noticeable drop at $r \sim 20$ kpc over $0^\circ < \theta < 45^\circ$, implying an apocentric boundary of debris stars from a merging progenitor galaxy of GSE. Additionally, the behaviors of α and q of the GSE-like subsample indicate the features of accreted halo components: its density distribution decreases more slowly with Galactocentric radius and it has a more spherical shape over $r < 20$ kpc than the general stellar halo sample.

We are grateful to the referee for the invaluable comments, which helped us to revise the current paper. We also thank Daniela Carollo for her many useful comments on the original manuscript. We acknowledge support from the JSPS and MEXT Grant-in-Aid for Scientific Research (Nos. 17H01101, 18H04434, and 18H05437).

Funding for the Sloan Digital Sky Survey IV has been provided by the Alfred P. Sloan Foundation, the U.S. Department of Energy Office of Science, and the Participating Institutions.

SDSS-IV acknowledges support and resources from the Center for High-Performance Computing at the University of Utah. The SDSS website is www.sdss.org.

SDSS-IV is managed by the Astrophysical Research Consortium for the Participating Institutions of the SDSS Collaboration, including the Brazilian Participation Group, the Carnegie Institution for Science, Carnegie Mellon University, Center for Astrophysics | Harvard and Smithsonian, the Chilean Participation Group, the French Participation Group, Instituto de Astrofísica de Canarias, The Johns Hopkins University, Kavli Institute for the Physics and Mathematics of the Universe (IPMU) / University of Tokyo, the Korean Participation Group, Lawrence Berkeley National Laboratory, Leibniz Institut für Astrophysik Potsdam (AIP), Max-Planck-Institut für Astronomie (MPIA Heidelberg), Max-Planck-Institut für Astrophysik (MPA Garching), Max-Planck-Institut für Extraterrestrische Physik (MPE), National Astronomical Observatories of China, New Mexico State University, New York University, University of Notre Dame, Observatório Nacional / MCTI, The Ohio State University, Pennsylvania State University, Shanghai Astronomical Observatory, United Kingdom Participation Group, Universidad Nacional Autónoma de México, University of Arizona, University of Colorado Boulder, University of Oxford, University of Portsmouth, University of Utah, University of Virginia, University of Washington, University of Wisconsin, Vanderbilt University, and Yale University.

This work has made use of data from the European Space Agency (ESA) mission Gaia (<https://www.cosmos.esa.int/gaia>), processed by the Gaia Data Processing and Analysis Consortium (DPAC; <https://www.cosmos.esa.int/web/gaia/dpac/consortium>). Funding for the DPAC has been provided by national institutions, in particular the institutions participating in the Gaia Multilateral Agreement.

ORCID iDs

Genta Sato  <https://orcid.org/0000-0002-0722-706X>
Masashi Chiba  <https://orcid.org/0000-0002-9053-860X>

References

- Anguiano, B., Majewski, S. R., Hayes, C. R., et al. 2020, *AJ*, **160**, 43
Antoja, T., Helmi, A., Romero-Gómez, M., et al. 2018, *Natur*, **561**, 360
Athanassoula, E. 2005, *MNRAS*, **358**, 1477
Bailer-Jones, C. A. L., Rybizki, J., Fousneau, M., Demleitner, M., & Andrae, R. 2021, *AJ*, **161**, 147
Batsleer, P., & Dejonghe, H. 1994, *A&A*, **287**, 43
Beane, A., Sanderson, R. E., Ness, M. K., et al. 2019, *ApJ*, **883**, 103
Beers, T. C., Drilling, J. S., Rossi, S., et al. 2002, *AJ*, **124**, 931
Bekki, K., & Chiba, M. 2000, *ApJL*, **534**, L89
Bekki, K., & Chiba, M. 2001, *ApJ*, **558**, 666
Bell, E. F., Naab, T., McIntosh, D. H., et al. 2006, *ApJ*, **640**, 241
Belokurov, V., Erkal, D., Evans, N. W., Koposov, S. E., & Deason, A. J. 2018, *MNRAS*, **478**, 611
Benson, A. J., Lacey, C. G., Frenk, C. S., Baugh, C. M., & Cole, S. 2004, *MNRAS*, **351**, 1215
Bignone, L. A., Helmi, A., & Tissera, P. B. 2019, *ApJL*, **883**, L5
Bond, N. A., Ivezić, Ž., Sesar, B., et al. 2010, *ApJ*, **716**, 1
Bovy, J. 2015, *ApJS*, **216**, 29
Bullock, J. S., & Johnston, K. V. 2005, *ApJ*, **635**, 931
Busso, G., Cacciari, C., Bellazzini, M., et al. 2021, in Gaia EDR3 Documentation (ESA; Gaia DPAC), <https://gea.esac.esa.int/archive/documentation/GEDR3/index.html>
Carollo, D., & Chiba, M. 2021, *ApJ*, **908**, 191
Carollo, D., Beers, T. C., Lee, Y. S., et al. 2007, *Natur*, **450**, 1020
Carollo, D., Beers, T. C., Chiba, M., et al. 2010, *ApJ*, **712**, 692
Carollo, D., Chiba, M., Ishigaki, M., et al. 2019, *ApJ*, **887**, 22
Chiba, M., & Beers, T. C. 2000, *AJ*, **119**, 2843
Chiba, M., & Beers, T. C. 2001, *ApJ*, **549**, 325
Conroy, C., Bonaca, A., Cargile, P., et al. 2019, *ApJ*, **883**, 107
Cooper, A. P., Parry, O. H., Lowing, B., Cole, S., & Frenk, C. 2015, *MNRAS*, **454**, 3185
Cooper, A. P., Cole, S., Frenk, C. S., et al. 2010, *MNRAS*, **406**, 744
Cordoni, G., Da Costa, G. S., Yong, D., et al. 2021, *MNRAS*, **503**, 2539
Cox, T. J., Dutta, S. N., Di Matteo, T., et al. 2006, *ApJ*, **650**, 791
Cui, X.-Q., Zhao, Y.-H., Chu, Y.-Q., et al. 2012, *RAA*, **12**, 1197
De Silva, G. M., Freeman, K. C., Bland-Hawthorn, J., et al. 2015, *MNRAS*, **449**, 2604
de Zeeuw, P. T., & Lynden-Bell, D. 1985, *MNRAS*, **215**, 713
de Zeeuw, T. 1985, *MNRAS*, **216**, 273
Deason, A. J., Belokurov, V., Koposov, S. E., & Lancaster, L. 2018, *ApJL*, **862**, L1
Deason, A. J., Fattahi, A., Belokurov, V., et al. 2019, *MNRAS*, **485**, 3514
Deason, A. J., Erkal, D., Belokurov, V., et al. 2021, *MNRAS*, **501**, 5964
Dejonghe, H., & de Zeeuw, T. 1988, *ApJ*, **333**, 90
Eadie, G., & Jurić, M. 2019, *ApJ*, **875**, 159
Eggen, O. J., Lynden-Bell, D., & Sandage, A. R. 1962, *ApJ*, **136**, 748
Evans, T. A., Fattahi, A., Deason, A. J., & Frenk, C. S. 2020, *MNRAS*, **497**, 4311
Fernández-Trincado, J. G., Beers, T. C., & Minniti, D. 2020, *A&A*, **644**, A83
Feuillet, D. K., Feltzing, S., Sahlholdt, C. L., & Casagrande, L. 2020, *MNRAS*, **497**, 109
Gaia Collaboration, Brown, A. G. A., Vallenari, A., et al. 2016, *A&A*, **595**, A2
Gaia Collaboration, Brown, A. G. A., Vallenari, A., et al. 2018, *A&A*, **616**, A1
Gaia Collaboration, Brown, A. G. A., Vallenari, A., et al. 2021, *A&A*, **649**, A1
Gillissen, S., Eisenhauer, F., Trippe, S., et al. 2009, *ApJ*, **692**, 1075
Grand, R. J. J., Deason, A. J., White, S. D. M., et al. 2019, *MNRAS*, **487**, L72
Hagen, J. H. J., Helmi, A., de Zeeuw, P. T., & Posti, L. 2019, *A&A*, **629**, A70
Helmi, A., Babusiaux, C., Koppelman, H. H., et al. 2018, *Natur*, **563**, 85
Ibata, R. A., Irwin, M. J., Lewis, G. F., Ferguson, A. M. N., & Tanvir, N. 2003, *MNRAS*, **340**, L21
Iorio, G., & Belokurov, V. 2019, *MNRAS*, **482**, 3868
Ivezić, Ž., Sesar, B., Jurić, M., et al. 2008, *ApJ*, **684**, 287
Jurić, M., Ivezić, Ž., Brooks, A., et al. 2008, *ApJ*, **673**, 864
Kim, B., & Lépine, S. 2022, *MNRAS*, **510**, 4308
Kim, Y. K., Lee, Y. S., Beers, T. C., & Koo, J.-R. 2021, *ApJL*, **911**, L21
Koppelman, H. H., Bos, R. O. Y., & Helmi, A. 2020, *A&A*, **642**, L18
Koppelman, H. H., Hagen, J. H. J., & Helmi, A. 2021, *A&A*, **647**, A37
Koppelman, H. H., Helmi, A., Massari, D., Price-Whelan, A. M., & Starkenburg, T. K. 2019, *A&A*, **631**, L9
Krujssen, J. M. D., Pfeffer, J. L., Chevance, M., et al. 2020, *MNRAS*, **498**, 2472
Lancaster, L., Koposov, S. E., Belokurov, V., Evans, N. W., & Deason, A. J. 2019, *MNRAS*, **486**, 378
Li, H., Du, C., Yang, Y., et al. 2020, *ApJ*, **895**, 23
Liang, X.-L., Chen, Y.-Q., Zhao, J.-K., & Zhao, G. 2021, *RAA*, **21**, 128
Mackereth, J. T., Schiavon, R. P., Pfeffer, J., et al. 2019, *MNRAS*, **482**, 3426
Majewski, S. R., Schiavon, R. P., Frinchaboy, P. M., et al. 2017, *AJ*, **154**, 94
May, A., & Binney, J. 1986, *MNRAS*, **221**, 857
McCarthy, I. G., Font, A. S., Crain, R. A., et al. 2012, *MNRAS*, **420**, 2245
Monachesi, A., Gómez, F. A., Grand, R. J. J., et al. 2019, *MNRAS*, **485**, 2589
Monty, S., Venn, K. A., Lane, J. M. M., Lokhorst, D., & Yong, D. 2020, *MNRAS*, **497**, 1236
Morganson, E., Conn, B., Rix, H.-W., et al. 2016, *ApJ*, **825**, 140
Mróz, P., Udalski, A., Skowron, D. M., et al. 2019, *ApJL*, **870**, L10
Myeong, G. C., Evans, N. W., Belokurov, V., Sanders, J. L., & Koposov, S. E. 2018a, *ApJL*, **863**, L28
Myeong, G. C., Evans, N. W., Belokurov, V., Sanders, J. L., & Koposov, S. E. 2018b, *ApJL*, **856**, L26
Myeong, G. C., Vasiliev, E., Iorio, G., Evans, N. W., & Belokurov, V. 2019, *MNRAS*, **488**, 1235
Naab, T., Khochfar, S., & Burkert, A. 2006, *ApJL*, **636**, L81
Naidu, R. P., Conroy, C., Bonaca, A., et al. 2020, *ApJ*, **901**, 48
Naidu, R. P., Conroy, C., Bonaca, A., et al. 2021, *ApJ*, **923**, 92
Newberg, H. J., Yanny, B., Rockosi, C., et al. 2002, *ApJ*, **569**, 245
Perryman, M. A. C., Lindegren, L., Kovalevsky, J., et al. 1997, *A&A*, **500**, 501
Posti, L., & Helmi, A. 2019, *A&A*, **621**, A56
Purcell, C. W., Bullock, J. S., & Kazantzidis, S. 2010, *MNRAS*, **404**, 1711
Rodríguez-Gomez, V., Pillepich, A., Sales, L. V., et al. 2016, *MNRAS*, **458**, 2371
Santistevan, I. B., Wetzel, A., El-Badry, K., et al. 2020, *MNRAS*, **497**, 747
Sestito, F., Longeard, N., Martin, N. F., et al. 2019, *MNRAS*, **484**, 2166

- Sofue, Y. 2020, [Galax](#), 8, 37
- Sommer-Larsen, J., & Zhen, C. 1990, [MNRAS](#), 242, 10
- Steinmetz, M., Zwitter, T., Siebert, A., et al. 2006, [AJ](#), 132, 1645
- Tissera, P. B., Scannapieco, C., Beers, T. C., & Carollo, D. 2013, [MNRAS](#), 432, 3391
- White, S. D. M., & Rees, M. J. 1978, [MNRAS](#), 183, 341
- Wyse, R. 2019, [Sci](#), 365, 979
- Yanny, B., Newberg, H. J., Grebel, E. K., et al. 2003, [ApJ](#), 588, 824
- Yanny, B., Rockosi, C., Newberg, H. J., et al. 2009, [AJ](#), 137, 4377
- Zhao, G., Zhao, Y.-H., Chu, Y.-Q., Jing, Y.-P., & Deng, L.-C. 2012, [RAA](#), 12, 723